



Kinetics and mechanistic insights into the acidic-basic active sites for water-containing catalytic hydrogenation of hydroxymethylfurfural over ceria-doped Ni/Al₂O₃

Brett Pomeroy^a, Miha Grilc^{a,*}, Sašo Gyergyek^b, Blaž Likozar^{a,*}

^a Department of Catalysis and Chemical Reaction Engineering, National Institute of Chemistry, Hajdrihova 19, 1000 Ljubljana, Slovenia

^b Department of Synthesis of Materials, Jožef Stefan Institute, Jamova Cesta 39, 1000 Ljubljana, Slovenia

ARTICLE INFO

Keywords:

Hydroxymethylfurfural
Hydrogenation
Biomass
Heterogeneous
Kinetics

ABSTRACT

This work presents a novel, systematic experimental and *in silico* study for hydroxymethylfurfural hydrogenation using ceria-doped Ni/Al₂O₃ catalysts with and without water-containing media. Despite improvements to reducibility, ceria-doped Ni/Al₂O₃ catalyst slowed reaction rates and TOFs relative to unpromoted Ni/Al₂O₃. Nonetheless, the NiCe/Al₂O₃ catalyst demonstrated enhanced ring opening and ring-saturation capability compared to unpromoted Ni/Al₂O₃ due to modifications of acidic-basic sites on the catalyst surface. Incorporating water as a co-solvent caused deoxygenation reactions to be essentially eliminated, resulting in 1,2,6-hexanetriol and 2,5-bishydroxymethyltetrahydrofuran as the only main products. Adsorbed water was determined to nullify oxygen vacancies and block strong acidic sites. Pretreating ceria under higher temperatures and in an oxygen-free atmosphere facilitated oxygen vacancy formation, leading to elevated dehydration in the absence of water. However, adding water into the system enhanced 1,2,6-hexanetriol formation and is anticipated to be dependent on the prevalence of basic sites that are associated with surface hydroxyls.

1. Introduction

Due to the recent shift towards more sustainable alternatives to combat the ongoing concerns of climate change, lignocellulosic biomass as a renewable feedstock has been considered to reach our global energy consumption needs in a more sustainable way. Cellulose, which comprises approximately half of all biomass, presents tremendous potential as a sustainable resource that can be converted to valuable bio-based chemicals and fuels. Specifically of interest has been the formation of 5-hydroxymethylfurfural (HMF) through the dehydration of glucose. HMF, which contains three versatile functional groups comprising of an aldehyde, alcohol, and furan ring, allows it to be converted to a wide range of highly valuable, industrially significant, chemical compounds. Particularly, 2,5-bishydroxymethyltetrahydrofuran (BHMTF) has been considered as a bio-based substitute in the manufacturing of certain polyesters and heat insulating polymers [1,2]. 1,2,6-hexanetriol (1,2,6-HT) can also be formed which is currently being applied as a moisturizing agent, solvent, and as a cross-linker in the polymer industry for the production of polyurethanes and synthetic rubbers. Additionally, 1,2,6-HT is an intermediate in the production of 1,6-hexanediol which is

used for numerous adhesive, coating, and paint applications. 1,6-hexanediol has enormous value with an estimated global market value of \$600 million USD, although presently has been exclusively made from fossil fuels with relatively low yields [3].

Catalytic hydrotreatment has been established as a suitable approach to convert HMF to these high-valued chemicals. Generally, this involves high hydrogen pressures (3 – 10 MPa), moderate temperatures up to 300 °C, and in the company of a heterogeneous solid catalyst. Regarding appropriate hydrogenation catalysts, transition metals such as nickel are preferred due to their lower cost relative to noble metals such as Pd and Pt, even though they typically provide inferior activity. Catalysts that incorporate an additional promoter metal are typically necessary to enhance catalyst activity and tune selectivity in the direction of more favourable products. Ceria as a promoter is usually applied for oxidation reactions due to its enhanced redox potential and ability to store oxygen [4–6]. Ceria utilized for hydrogenation reactions is more infrequent in the literature, but its ability to evoke both acidic-basic functionalities (amphoteric), improve metal dispersion through inhibiting metal sintering, and its resistance to water makes ceria an interesting promoter for such biomass conversion processes [7–10].

* Corresponding authors.

E-mail addresses: miha.grilc@ki.si (M. Grilc), blaz.likozar@ki.si (B. Likozar).

<https://doi.org/10.1016/j.apcatb.2023.122868>

Received 15 March 2023; Received in revised form 5 May 2023; Accepted 8 May 2023

Available online 9 May 2023

0926-3373/© 2023 The Authors. Published by Elsevier B.V. This is an open access article under the CC BY-NC-ND license (<http://creativecommons.org/licenses/by-nc-nd/4.0/>).

As shown in Table 1, several studies have previously achieved high selectivities of both BHMTF and 1,2,6-HT, although a comprehensive understanding of their intrinsic reaction kinetics has been particularly inadequate in the literature. Kinetic modelling can offer vital information for a more complete understanding of surface chemistry on a fundamental level, which is not conceivable through conventional methods. Grounded on first-principles, kinetic models take into account several important elementary steps within the reaction system including adsorption and desorption kinetics, gas solubility in the liquid phase, and catalyst surface reactions. Kinetic studies on the catalytic conversion of HMF are few and far between in the literature and the ones that are reported are based on rudimentary systems that provide limited knowledge [11,12]. A comprehensive kinetic model for the hydrogenation of HMF remains insufficient, therefore this study aims to complement and expand our previous work on carbon-based catalysts [13] to develop a more thorough kinetic model using promoted alumina-supported catalysts. Kinetic studies that provide mechanistic understanding are of utmost importance to realize optimal operating reaction conditions and catalyst design to obtain maximum yields of a desired product.

This study presents a kinetic model for the hydrogenation of HMF in a batch regime at applicable reaction temperatures (140–200 °C), which includes all liquid-phase intermediate and product concentrations as a function of time. Relying on experimental data and detectable products, a detailed reaction network is offered alongside a comprehensive kinetic scheme to model the experimental conclusions and calculate relevant kinetic parameters including reaction rates, activation energies, and turnover frequencies (TOFs). HMF hydrogenation was studied in THF with and without water as these solvent systems have been proven to be selective for C₆ sugar conversion towards HMF [18,24]. Furthermore, we propose that water may play an overlooked role in hydrogenation reactions for tuning product selectivity by protecting the catalyst surface and/or metal-support interface sites from adsorption of certain reaction intermediates and/or products [12,25]. Additionally, the influence of oxygen vacancies on product selectivity was investigated by altering the pretreatment environment of the ceria during synthesis to methodically investigate the determining factors on catalyst activity and product selectivity. Oxygen vacancies amongst ceria catalysts has long been considered to play a major role in surface reactions and can influence catalyst activity and product selectivity [26–28].

2. Experimental

2.1. Materials

All chemical reactants, calibration standards, and gases were purchased commercially and were used without further purifications; 5-Hydroxymethylfurfural (>97 wt%, Carbosynth, reference number FH10853), 5-methylfurfural (99 wt%, Sigma Aldrich), dimethylfuran

(99 wt%, Sigma Aldrich), 2,5-bis(hydroxymethyl)furan (98 wt%, VWR), 2,5-bis(hydroxymethyl) tetrahydrofuran (>95 wt%, Carbosynth), (5-methyl-2-furyl)methanol (98 wt%, Carbosynth), 1,2,6-hexanetriol (96 wt%, Sigma Aldrich), 1,5-pentadiol (96 wt%, Sigma Aldrich), 2-hexanol (99 wt%, Sigma Aldrich), hydrogen (5.0, Messer, Germany), nitrogen (5.0, Messer, Germany), NH₃ (5 vol% in He, Germany), helium (5.0 Messer, Germany), carbon monoxide (5 vol% CO in He, Linde, Germany), and tetrahydrofuran (>95 wt%, EMD Millipore) was used as solvent. Nickel (II) nitrate hexahydrate (97 wt%, Sigma-Aldrich, USA, reference number 72253), and cerium (III) nitrate hexahydrate (99 wt%, Sigma-Aldrich, USA) were implemented in catalyst preparation using γ -alumina (Spheralite 537, Procatalyse, France) as support.

2.2. Catalyst Preparation

Solid catalysts were prepared by incipient wetness impregnation using specific aqueous solutions of Ni(NO₃)₂•6 H₂O and Ce(NO₃)₃•6 H₂O. Before impregnation, the γ -alumina support was crushed and sieved to acquire the 40 – 100 μ m fraction. Following each impregnation, catalysts were dried in an oven overnight at 110 °C, then pretreated accordingly. Promoted NiCe catalysts were impregnated sequentially, ceria was added first, dried at 110 °C, then pretreated at 400 °C or 800 °C for 4 h in air or nitrogen atmospheres, and then successively nickel was added. Ni was consistently calcined in air at 400 °C for 4 h for both Ni-containing unpromoted and promoted catalysts. Catalyst compositions were kept consistent with 10 wt% Ni and/or 15 wt% Ce. Incipient wetness impregnation was chosen as it was expected that nickel would not fully incorporate into the ceria lattice, as reported elsewhere [29]. Catalysts are referred to throughout the text according to their metal loading (10Ni or 10Ni15Ce), ceria pretreatment temperature (400 or 800), and pretreatment environment (A for air, N for nitrogen). For example, 10Ni15Ce 400 A refers to the catalyst with 10 wt% Ni and 15 wt% Ce where the ceria was pretreated at 400 °C in air.

2.3. Catalyst characterization

2.3.1. Surface and textural properties

Blank supports and doped catalysts were analyzed via nitrogen physisorption to determine average pore diameter (d_p), pore volume (V_p), and specific surface area (S_{BET}) using an ASAP 2020 gas adsorption instrument (Micrometrics, USA). Field-emission scanning electron microscopy (FE-SEM) (SUPRA 35 VP, Carl Zeiss, Germany) was performed to observe morphological properties. Transmission Electron Microscopy (TEM) was implemented at 200 kV with a thermionic electron-source TEM JEOL JEM 2010 F where samples were deposited on a copper-grid-supported lacy carbon foil. Chemical composition was analyzed using an Oxford Instruments ISIS 300 EDXS spectrometer. X-ray diffraction (XRD) patterns were characterized with a PW3040/60 X'Pert PRO MPD diffractometer at 35 kV and 45 mA with Cu K α radiation

Table 1
Comparison of hydrogenation of 5-hydroxymethylfurfural over related catalysts.

Catalyst	Solvent	Temp. (°C)	Pres. (MPa)	Conv. (%)	Selectivity (%) (BHMF, BHMTF, 1,2,6-HT)			Ref.
20 mol% Cu/Al ₂ O ₃	MeOH	130	3	100	93	0	0	[14]
3 wt%N + 5 wt%Re/TiO ₂	H ₂ O	40	5	95	84	0	0	[15]
1 wt% Au/Al ₂ O ₃	H ₂ O	60	6.5	100	96	0	0	[16]
5 wt% Ru/C	H ₂ O	140	7	100	0	89	0	[17]
1 wt% Ru/CeO ₂	1-BuOH/H ₂ O	130	2.8	100	0	91	3	[18]
74 wt% Ni/Al ₂ O ₃	1,4-dioxane	60	6	100	4	96	0	[19]
Raney Ni (>93 wt%)/Al ₂ O ₃	1,4-dioxane	100	1.5	100	0	96	0	[20]
7 wt%Ni+ 5 wt%Ga/Al-LDO	THF	140	3	100	0	99	0	[21]
1 wt% Ru/C	1-BuOH/H ₂ O	130	2.8	100	0	53	13	[18]
5 wt%Pt/CeO ₂	H ₂ O	135	3	100	0	63	27	[22]
10 wt%Ni+ 15 wt%Ce/Al ₂ O ₃	THF/H ₂ O	140	5	100	96	4	0	Previous work[23]
	1-BuOH	190	5	100	0	88	9	Previous work[23]
	THF/H ₂ O ^a	190	5	100	2	39	59	Previous work[23]

^a Addition of CaO

source ($\lambda = 0.154056$ nm) in the 2θ range from 10° to 80° applying JCPDS database for reference. X-ray photoelectron spectroscopy (XPS) analysis was conducted on a PHI-TFA XPS spectrometer (Physical Electronics Inc.) equipped with X-ray Al-monochromatic source. A low energy electron gun was implemented to avoid sample charging. XPS spectrum O 1 s was aligned to the binding energy 531.0 eV, characteristic of Al_2O_3 , to account for potential charging effects. Quantification of the surface composition was performed from XPS peak intensities considering relative sensitivity factors provided by instrument manufacturer [30]. Resulting spectrums were evaluated using Multipak program version 9.9 which were fitted with Gauss-Lorentz functions and Shirley function was used for background removal. X-ray fluorescence spectrometer (ED-XRF) with a Ge semiconductor detector was utilized to determine if any metal species leached into the liquid phase during activity tests.

2.3.2. Hydrogen-temperature programmed reduction

Hydrogen temperature-programmed reduction (H_2 -TPR) was carried out with a Micrometrics AutoChem II Chemisorption Analyser (Micrometrics, Norcross, USA). Firstly, a 100 mg sample of catalyst was positioned into a quartz U-tube and pretreated under a 50 mL min^{-1} flow of argon at 300°C for 60 min with a heating rate of 30 K min^{-1} prior to reduction. Subsequently, the sample then underwent 40 mL min^{-1} of a 5 vol% H_2 in Ar mixture at a constant heating rate of 10 K min^{-1} up to a maximum of 800°C . Hydrogen consumption was estimated using a TCD detector previously calibrated with CuO .

2.3.3. NH_3 / CO / CO_2 / H_2O -temperature programmed desorption

All temperature programmed desorption (TPD) analysis was performed on the same apparatus as TPR. Preceding TPD measurements, 100 mg catalyst samples were initially pretreated under the identical reduction conditions implemented for catalytic activity tests (400°C for 3 h). Samples were subjected to 80 mL min^{-1} of ammonia or carbon dioxide mixtures (10 vol% NH_3 or 10 vol% CO_2 in He) at 60°C before being purged with He and heated with a constant heating rate of 5 K min^{-1} . To quantify metallic sites, CO pulse chemisorption was conducted by pulsing 5 vol% CO in He at -80°C before heating up to 600°C with a constant heating rate of 5 K min^{-1} . During H_2O -TPD, pure Ar (80 mL min^{-1}) was purged through the water for adsorption. A TCD was implemented to detect desorbed compounds and ideal mass spectrums were identified with a GSD 301 T3 Thermostar Mass Spectrometer. Calibration gas mixtures of known concentrations were utilized to estimate metallic, basic, and acid sites. Diffuse reflectance infrared Fourier transform (DRIFT) experiments were obtained with a DiffusIR cell (PIKE Technologies) coupled to Perkin Elmer Frontier spectrometer using pyridine as the probe molecule. 20 mg samples of catalyst were initially pre-treated for 20 min in a 100 mL min^{-1} flow of N_2 at 350°C , cooled to room temperature, then saturated with pyridine vapour in a 50 mL min^{-1} flow of N_2 gas stream for 10 min and subsequently evacuated for 10 min. Temperature-programmed DRIFT experiments were also performed using CO_2 as the probe molecule. Prior to CO_2 adsorption, catalyst samples were reduced in situ at 400°C for 3 h in hydrogen. Then after flushing with Ar, pulses of CO_2 were injected at room temperature until saturation, then flushed again with Ar until gaseous CO_2 was removed from the cell before heating up the samples. The spectra collected are the average of 32 scans with a resolution of 4 cm^{-1} and over a $1000 - 4000\text{ cm}^{-1}$ wave number range.

2.4. Catalytic activity tests

Catalytic activity tests were performed in 75 mL stainless steel batch reactors (Parr 5000 Series) with a magnetic stir bar for mixing. Agitation of 1000 rpm with a magnetic stir bar ensured sufficient mixing for complete dispersion of the catalyst particles to minimize external mass transfer effect amongst gas-liquid-solid phases. Each reaction contained 0.1 g of solid catalyst (pre-reduced weight), 1 g of HMF, and THF with

and without Milli-Q water to maintain a constant total volume of 40 mL. Before activity tests, catalysts were reduced in a pure hydrogen flow of 40 mL min^{-1} at 400°C for 3 h with a heating rate of 10 K min^{-1} . The influence of reaction temperature was investigated in the range of $140 - 200^\circ\text{C}$ with a heating rate of 5 K min^{-1} and reactions lasted 6 h starting when the desired reaction temperature was reached. Once the reactant, solvent(s) and catalyst(s) were weighed in appropriate amounts and placed in the reactor vessel and sealed, each autoclave was purged with inert atmosphere (N_2) three times to remove any air in the vessel, then pressurized with 5.0 MPa of H_2 to maintain an approximate $\text{H}_2:\text{O}$ ratio of 20:1. Liquid samples were collected once the desired reaction temperature was obtained, then at every hour thereafter during isothermal conditions from the same experiment. Immediately after the reaction was completed, the autoclave was rapidly cooled down in water. When the temperature reached below 30°C , the pressure was released from the reactor before opening to collect the spent catalysts.

Spent catalysts were applied for recyclability tests after the first activity test. After the first reaction, spent catalysts were filtered from the liquid phase, washed with THF and centrifuged twice, dried in a nitrogen atmosphere, and then pretreated in hydrogen under equivalent conditions as prior (400°C for 3 h, 40 mL min^{-1}) before being subjected to another activity test. Following two recycled tests (R1-R2), spent catalysts were washed similarly with THF, then underwent calcination in air at 400°C for 2 h. Spent catalysts were then reduced under equivocal conditions as prior for R3 recycled test.

2.5. Product Analysis

Collected liquid products were filtered by $0.22\text{ }\mu\text{m}$ PET syringe filters before being analyzed by gas chromatography with flame ionization detector (GC-FID) (Nexis GC-2030, Shimadzu). Liquid product compounds were separated by Zebron ZB-5MS capillary column ($60\text{ m} \times 0.25\text{ mm} \times 0.25\text{ }\mu\text{m}$, Phenomenex, CA, USA) and identified with a mass spectrometer. GC analysis parameters were set with an initial oven temperature of 60°C and then heat-up to match the injector temperature of 290°C . Quantification for each product was determined with commercially purchased external standards. The catalytic activity test with 10Ni catalyst at 190°C in THF: 5 vol% water was performed in triplicate to validate the reproducibility of catalytic activity tests. Mean concentrations of the triplicates are shown in Figure S.1 and standard deviations of the mean are shown as error bars. The average standard deviation of the mean for all products was 0.004. The carbon balance for liquid products for all activity tests were consistently above 91%.

3. Results and discussion

3.1. Catalyst characterization

3.1.1. Surface and textural properties

Nitrogen physisorption analysis results are displayed in Table 2. Associated nitrogen adsorption-desorption isotherms presented in Figure S.2 of the blank alumina support and doped catalysts exhibited comparable isotherm characteristics. Impregnation with nickel and/or ceria decreased specific surface area (S_{BET}), average pore diameter (D_p), and average pore volume (V_p) moderately relative to the bare support, signifying that some blocking of the catalyst pores occurred. In terms of the promoted nickel catalysts, pretreating the catalyst at 800°C in either atmosphere (N_2 or air) resulted in considerably lower S_{BET} and greater D_p compared to catalysts pretreated at 400°C , likely due to the partial closure of some smaller pores at higher pretreatment temperatures. This aligns with what has been reported elsewhere where increasing calcination temperature caused an increase in ceria particle size and lowered catalyst surface area [4]. Furthermore, pretreating in air instead of nitrogen also seemed to preserve porosity with higher V_p and lower D_p at both pretreatment temperatures.

SEM images of the blank support, reduced 10Ni and 10Ni15Ce

Table 2Textural properties obtained from N₂ Physisorption.

Sample	S _{BET} (m ² g ⁻¹)	t-plot micropore area (m ² g ⁻¹)	t-plot external surface area (m ² g ⁻¹)	Avg. pore volume (cm ³ g ⁻¹)	Avg. pore diameter (nm)
Bare	185	10	175	0.51	8.6
γ-Al ₂ O ₃					
10Ni	172	8	164	0.42	7.7
15Ce 400 A	165	2	163	0.40	7.7
10Ni15Ce 400 A	160	5	155	0.38	7.5
10Ni15Ce 400 N	152	2	150	0.34	7.4
10Ni15Ce 800 A	121	6	115	0.35	9.0
10Ni15Ce 800 N	122	6	116	0.32	8.5

catalysts, as well as spent 10Ni15Ce catalyst are displayed in Figure S.3. The relative high porosity of the alumina support can be clearly seen with most pores being < 10 nm. From external observation, the unpromoted Ni and promoted NiCe catalyst appear to be relatively analogous in surface textural properties with no obvious differences. This also aligns with the results determined with N₂ physisorption analysis where both catalysts demonstrated comparable BET specific surface areas, average pore volume, as well as average pore diameters as reported in Table 2. As displayed in Figure S.4, TEM analysis of the reduced Ni on Al₂O₃ reveals that the alumina is in the form of approx. micron-sized agglomerates of ~10 nm sized nanocrystals (encircled area in Figure S.4 (b)). EDXS analysis reported in our previous work [23] demonstrated that alumina is uniformly decorated with Ni, however, distinct Ni particles are not visible at any magnification. Darker areas seen in Figure S.4 (a) are alumina nanocrystals oriented in such a way to strongly diffract the electron beam and thus, is seen as darker areas in bright field images. It is estimated that the size of Ni species is significantly below 1 nm (vide supra). Contrarily, CeO₂ is observed to be present as ~10 nm nanocrystals that are homogeneously distributed over the alumina support (Figure S.4 (c) and (d)) with a lattice fringe of 0.316 nm, indicating (111) crystal plane. High-resolution imaging (Figure S.4 (d)) further confirms that darker particles clearly visible in Figure S.4 (c) are CeO₂ nanocrystals. Promoted 10Ni15Ce catalysts pretreated under various conditions appear to be very similar (Figure S.5 (a-h)) in which all are composed of approximately 10 nm-sized CeO₂ nanocrystals uniformly distributed over the alumina. CeO₂ is well crystalline and does not grow substantially during the reduction process (Figure S.5, right column). Despite the varied pretreatment, distinctive Ni nanoparticles are not visible in any sample.

XRD profiles for unpromoted and promoted nickel-based catalysts with different pretreatments are shown in Fig. 1. The γ-alumina support contained a broad peak between 30° and 40° (311), and two sharper peaks at 46° (400) and 67° (440) which are associated with gamma phase planes of alumina (JCPDS# 00-048-0367) [9,31]. Diffraction peaks correlating with the typical fluorite cubic cell of CeO₂ are evidently present in all ceria-doped catalysts (JCPDS# 00-004-0593). XRD spectra of pure ceria oxide was included for comparative purposes which demonstrated peaks at 28° (111), 33° (200), 48° (220), 56° (311), 59° (222), 70° (400), 77° (331), 79° (420). Diffraction lines corresponding to NiO (JCPDS# 04-0850) or nickel containing alloys were not present in any unpromoted or promoted Ni-based catalyst sample regardless of pretreatment. This is to be expected, as the NiO species are likely below detection limit according to TEM images.

3.1.2. XPS

X-ray photoelectron spectroscopy (XPS) was applied to determine composition as well as identify oxidation states of detected elements on

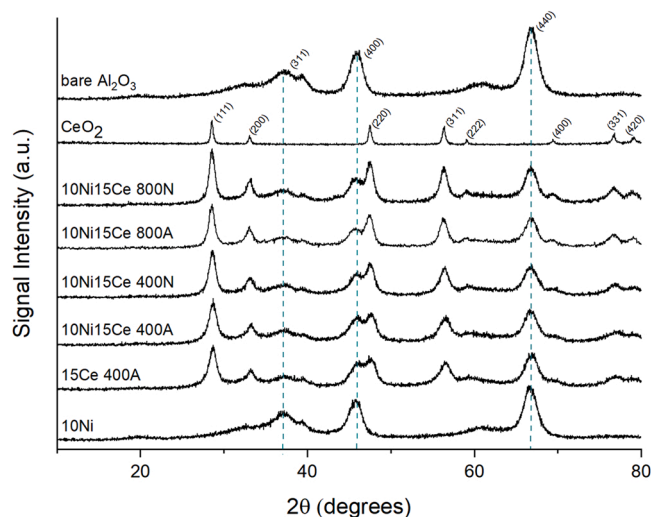


Fig. 1. XRD spectra of unpromoted and promoted Ni-based catalysts along with bare alumina and cerium oxide for comparative purposes.

the catalyst surface, generally within the top 3–5 nm [9]. Figure S.7 displays the general XPS spectra obtained of the 10Ni15Ce 400 A catalyst where peaks C 1 s, O 1 s, Al 2p, Al 2 s, Ni 2p, Ce 3d, O KLL, and Ni LMM were observed. Surface composition of the promoted NiCe catalysts were also estimated based off of XPS spectra, as shown in Table S.1. Results suggest that surface oxygen declined as pretreatment temperature increased and when performed in a nitrogen atmosphere. This aligns with literature where a similar loss in surface oxygen was observed when pretreating ceria in the absence of oxygen and at higher temperatures [32,33]. The considerably low surface concentrations of Ce indicate that the vast majority of the ceria is either blocked by Ni, or has migrated relatively deep into the alumina lattice. Low surface concentrations of nickel (relative to the nominal 10 wt% that was added during synthesis) also suggests that some Ni species migrates into the alumina and/or ceria, but is not as prevalent at higher pretreatment temperatures (~3.6% at 400 °C vs. ~6.0% at 800 °C).

Deconvoluted XPS spectra obtained for Ce 3d and Ni 2p of the promoted NiCe catalysts are presented in Fig. 2. The Ni 2p spectra, assigned to Ni²⁺ oxidation state, comprises 4 peaks; i) Ni 2p_{3/2} at 855.6 eV, ii) Ni 2p_{3/2} satellite peak at 861.2 eV, iii) Ni 2p_{1/2} peak at 873.5 eV, and iv) Ni 2p_{1/2} satellite peak at 879.1 eV. These binding energies correspond with Ni²⁺ belonging to Ni(OH)₂ species [34,35]. Several peaks were observed for Ce oxides denoted by 'u' for Ce 3d_{5/2}, and 'v' for Ce 3d_{3/2}. As reported elsewhere, these peaks indicate the presence of both Ce³⁺ (labelled as v' and u') and Ce⁴⁺ (labelled as v, u, v'', u'', v''', and u''') oxidation states [36–38]. Due to considerable overlapping between both Ce and Ni peaks, in addition to the low composition of surface Ce, it was not possible to quantify exact amounts of Ce⁴⁺/Ce³⁺. Nonetheless, it is clearly seen that peaks v''' and v, directly correlated to the concentration of Ce⁴⁺, was the highest when pretreated at 400 °C in air and followed the trend; 400 A > 400 N > 800 A > 800 N. This is in perfect accordance with the composition of oxygen on the catalyst surface and relates directly to the increased presence of Ce³⁺ that is formed with the emergence of oxygen vacancies. This aligns well with literature reporting that ceria releases more oxygen with higher pretreatment temperature and lower partial pressures (or absence) of oxygen [39,40].

3.1.3. Hydrogen temperature programmed reduction

H₂-TPR profiles of the bare alumina support, unpromoted Ce and Ni doped catalysts, nickel and cerium oxides, as well as promoted NiCe catalysts are shown in Fig. 3. The bare γ-alumina support demonstrated negligible reducibility. The 10Ni catalyst demonstrated the typical strong interaction between the Ni and Al₂O₃ support with the

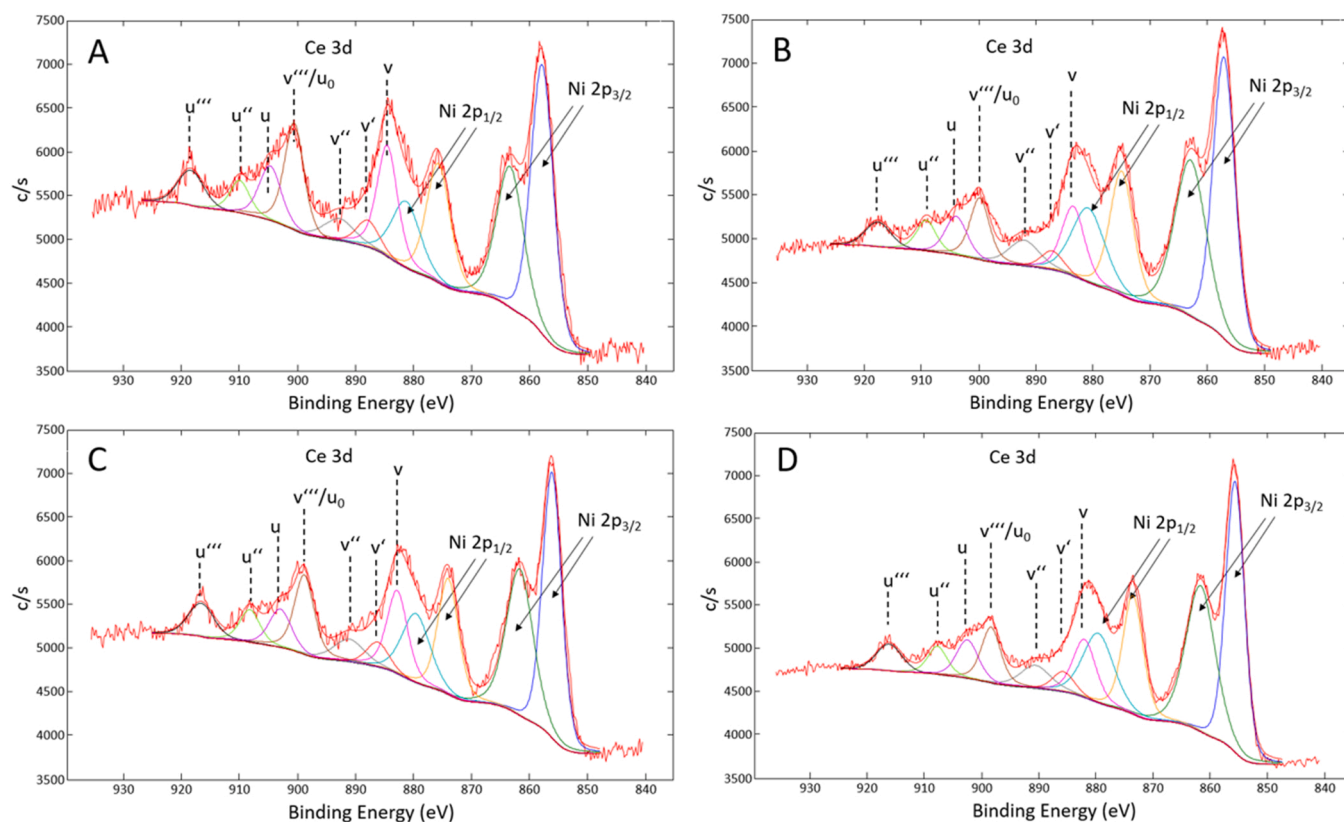


Fig. 2. Deconvolution of Ce 3d and Ni 2p spectra from catalysts (A = 10Ni15Ce 400 A, B = 10Ni15Ce 800 A, C = 10Ni15Ce 400 N, and D = 10Ni15Ce 800 N).

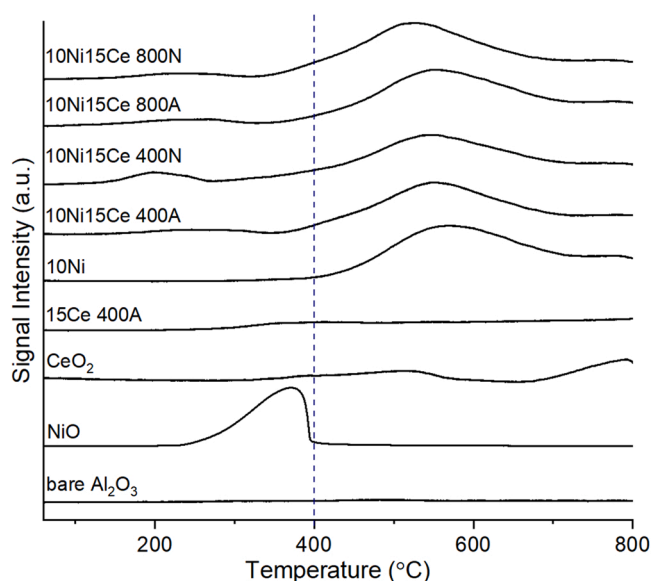


Fig. 3. H₂-TPR profiles of bare support, metal oxides, and doped γ -alumina catalysts.

characteristic reduction profile encompassing a large amount of NiAl₂O₄ spinels that reduce at elevated temperatures centered around 550 °C [41]. Reduction of pure CeO₂ revealed modest hydrogen consumption with a broad peak between 350 °C and 550 °C, correlating to surface oxygen reduction of CeO₂, and a second peak beginning at 700 °C corresponding to the reduction of bulk ceria [42–44]. However, when ceria was impregnated onto the alumina support, reducibility was essentially abolished. This behavior aligns with what has been reported elsewhere

in which ceria can incorporate itself into the alumina lattice as a result of the strong interaction between the two, stabilizing as Ce-O-Al bonds to form CeAlO₃ [10,45,46]. The occurrence of CeAlO₃ has been described to weaken the interaction that typically transpires between nickel and alumina, restraining the crystalline growth of NiO species and thus, improving dispersion and reducibility of the active metal [47,48]. This behaviour agrees with the TPR profiles of all promoted NiCe catalysts which unanimously demonstrated enhanced reducibility relative to the unpromoted Ni catalyst due to the emergence of a broad peak centralized around 225 °C and a slight shift in the NiAl₂O₄ peak to lower temperatures. Minor differences in reducibility were observed between the diverse pretreatment methods including the 10Ni15Ce 400 N catalyst having a narrower profile relative to the others around 200 °C (Fig. 3). TPR analysis of pure NiO resulted in a major peak between 240 °C and 400 °C that is accredited to the complete reduction of NiO (Ni²⁺) to Ni⁰ [49,50]. Thus, all catalysts were reduced at 400 °C prior to activity tests to ensure species corresponding to NiO were largely reduced.

3.2. Acid, Basic, and Metallic Sites Determination

Ammonia, carbon dioxide, and carbon monoxide temperature-programmed desorption coupled to a mass spectrometer (NH₃ /CO₂ /CO-TPD-MS) was conducted to determine the relative strength and to quantify the total number of acid, basic, and metallic sites, respectively, as displayed in Table 3. Carbon monoxide temperature-programmed desorption coupled with a mass spectrometer (CO-TPD-MS) was performed to quantify the concentration of metallic active sites based on mass spectrums corresponding to CO ($m/z = 28$ with deduction from CO₂ contribution). Overall, the promoted 10Ni15Ce catalysts contained relatively more metallic sites (181 – 206 $\mu\text{mol g}^{-1}$) relative to the unpromoted 10Ni catalyst (116 $\mu\text{mol g}^{-1}$), correlating with the improved reducibility that was observed in H₂-TPR (Fig. 3). Mass

Table 3Quantitative results for NH₃, CO, and CO₂ desorption and calculated concentration of sites.

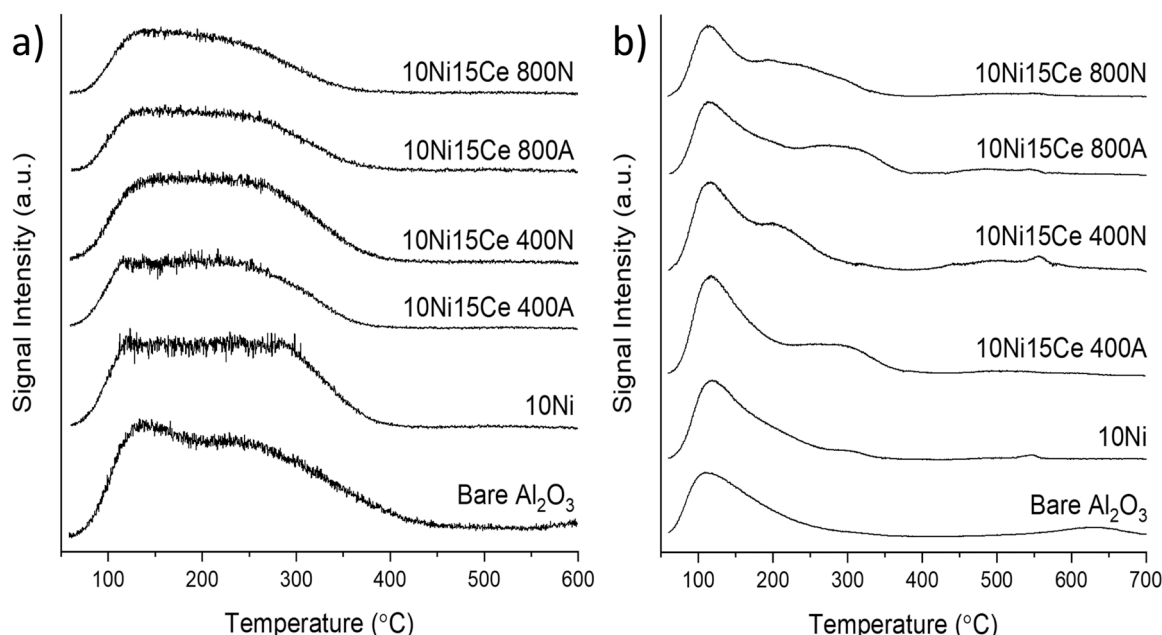
Sample	Volume of NH ₃ (mL)	Conc. Of Acidic sites (μmol g ⁻¹)	Volume of CO (mL)	Conc. Of Metallic sites (μmol g ⁻¹)	Volume of CO ₂ (mL)	Conc. Of Basic sites (μmol g ⁻¹)	Ratio of Acid to basic
γ-Al ₂ O ₃	1.13	546	N/A	N/A	0.16	72	N/A
10Ni	0.98	439	0.27	116	0.19	86	5.1
15Ce 400 A	0.90	404	N/A	N/A	0.17	78	N/A
10Ni15Ce 400 A	0.71	318	0.44	188	0.28	130	2.5
10Ni15Ce 400 N	0.85	381	0.42	181	0.25	115	3.3
10Ni15Ce 800 A	0.70	312	0.46	197	0.17	80	3.9
10Ni15Ce 800 N	0.79	353	0.48	206	0.16	73	4.8

Experimental error for NH₃, CO, CO₂ desorption values was established to be ± 10%.

spectroscopy profiles of NH₃-TPD, shown in Fig. 4a, correspond to $m/z = 15$ to isolate desorbed ammonia from water which both have m/z of 17. Initially, an NH₃-TPD of the blank alumina support indicated substantial acidity with 546 μmol g⁻¹ acid sites ranging from 75 °C to 420 °C, indicating the presence of a wide strength range of acid sites. Doping the alumina with Ce and/or Ni decreased the total concentration of acid sites compared to the bare alumina support. The different pretreatments of ceria amongst the promoted 10Ni15Ce catalysts altered the total concentration of acid sites, though the acid strength remained relatively unaffected. The order of highest acidity to lowest acidity was as followed; 400 N > 800 N > 400 A ≈ 800 A. This trend indicates that pretreating the ceria in nitrogen results in considerably higher concentration of acidic sites compared to pretreating in air. This is similar to what has been reported elsewhere where oxygen vacancies can attribute to increased acidity [51]. Diffuse reflectance infrared Fourier transform (DRIFT) FTIR analysis with pyridine as a probe molecule determined that both 10Ni and 10Ni15Ce catalysts demonstrated almost exclusively Lewis acidity with two main peaks at 1448 and 1605 cm⁻¹ (Figure S.8). This is to be expected as Al³⁺, Ni²⁺, and cerium cations Ce³⁺ and Ce⁴⁺ are all Lewis acidic in nature [52–55].

Carbon dioxide temperature-programmed desorption coupled with a mass spectrometer (CO₂-TPD-MS) was performed to quantify the concentration of basic sites on the catalyst surface and mass spectrums

associated with CO₂ ($m/z = 44$) are also displayed in Fig. 4b. Table 3 indicates that total basic sites amongst the promoted 10Ni15Ce catalysts decreased in the order of 400 A > 400 N > 800 A > 800 N, analogous to the trend of increased oxygen vacancies realized during XPS (Table S.1). It is well-known that basic sites are directly related to the O²⁻ species within the catalyst [56,57]. Three main CO₂ desorption peaks are present which include a large peak centered around 114 °C, a peak centered around 196 °C, and a broad peak between 250 °C and 367 °C. To better understand and identify what these peaks were associated with on the catalyst surface, temperature-programmed DRIFT experiments were performed on catalysts using CO₂ as the probe molecule, and the resulting IR spectra are shown in Figure S.9. The bare γ-Al₂O₃ support as well as all doped catalysts demonstrated three adsorption bands at 1659 cm⁻¹, 1435 cm⁻¹, and 1227 cm⁻¹ which are indicative of bicarbonates from CO₂ interacting with basic surface hydroxyls [58–61]. These bicarbonates correspond to the first peak centered around 114 °C, and are attributed to weak basic sites. The 10Ni catalyst had a total number of basic sites closer to those of the 10Ni15Ce catalysts pretreated at 800 °C, though essentially only comprised of weaker basic sites like the bare alumina support. The resulting IR spectra of the 10Ni catalyst did not exhibit any additional peaks compared to the bare alumina, indicating that CO₂ did not adsorb onto any nickel species. The incorporation of ceria facilitated the formation of stronger basic sites relative

Fig. 4. a. NH₃-TPD-MS profiles ($m/z = 15$), and Fig. 4b. CO₂-TPD-MS profiles ($m/z = 44$).

to the unpromoted 10Ni catalysts. All 10Ni15Ce catalysts displayed some moderate strength basicity around 196 °C peak. Correspondingly, the same catalysts all displayed an adsorption band at 1390 cm^{-1} which could correspond to bridged carbonates on ceria [62,63]. The stronger basic sites up to 367 °C that presented with the promoted 10Ni15Ce catalysts pretreated in air are likely adsorbed formate species (1371 cm^{-1} and 1592 cm^{-1}) [64–66]. Bicarbonates, as the most abundant basic site, significantly decreases as pretreatment temperature was increased to 800 °C. This is to be expected as bicarbonates are recognized to form via dehydration reactions between surface –OH and CO_2 which occur more readily at elevated temperatures [60].

3.3. Reaction pathway network and kinetic model development

Liquid products detected and verified by GC-FID/MS under our reaction conditions over nickel-based alumina catalysts were identified to be; 2,5-bis(hydroxymethyl)furan (BHMF), 2,5-bis(hydroxymethyl)tetrahydrofuran (BHMTHF), (5-methyl-2-furyl)methanol (2-HM-5-MF), 5-methyltetrahydrofurfuryl alcohol (MTHFA), 1,2,6-hexanetriol (1,2,6-HT), furfuryl alcohol (FA), tetrahydrofurfuryl alcohol (THFA), 1,5-pentadiol (1,5-PD), and 1,5-hexanediol (1,5-HD). Trace amounts of 5-methylfurfural (5-MF), dimethylfuran (DMF), dimethyltetrahydrofuran (DMTHF), and 2-hexanol (2-HXL) were also observed. Prior to establishing the kinetic model, a comprehensive reaction network has been presented in Fig. 5 which was founded on the detected intermediates and products during activity tests. Colours offered for each compound presented in the reaction pathway correlate with the colours presented later in Figs. 6–9 that report liquid product concentration profiles as a function of time. To validate the incidence of competing and parallel reactions, activity tests utilizing intermediates BHMF and 1,2,6-HT, in addition to a final reaction mixture were completed. Blank Al_2O_3 resulted in no detectable activity (Fig. 6h). Additionally, applying the 15Ce catalyst demonstrated negligible activity when starting with either HMF (Fig. 7h) or BHMF (Fig. 8h), signifying that Ni metallic sites are imperative for catalyst activity. As shown in Fig. 9h, neither FA nor THFA were detected when using BHMF as the starting reagent, verifying that they arise from the direct decarbonylation of HMF. It was not possible to convert BHMTHF further, even when subjecting a final mixture to an additional 6 h reaction under the same conditions with a newly reduced catalyst (Figure S.10b), indicating that the formation of 1,2,6-HT and BHMTHF are in parallel rather than in series, similar to what has been reported elsewhere [67,68]. An activity test was then

carried out starting from 1,2,6-HT which confirmed the formation of 1,5-PD to transpire via C-C cleavage of 1,2,6-HT (Figure S.10a). This result was rather unexpected since it would be anticipated that the C-C bond would require substantially high energy to cleave. This was reported elsewhere using CuCr catalyst with similar yields, though they applied harsher reaction conditions of 260 °C and 100 bar of H_2 [69]. Neither 1,5-HD or 2-HXL were detected when beginning with 1,2,6-HT. Based on these conclusions, we advocate that all other ring opened products (1,5-HD and 2-HXL) are formed via intermediates comprising unsaturated furan rings (2-HM-5-MF and DMF), also aligning with what has been described by several other studies [70–72]. Grounded from these results and activity tests, we have confidence in our offered reaction network where all other ring-opened products originate via intermediates containing unsaturated furan rings.

The presented kinetic model outlines a three-phase (gas-liquid-solid) system that accounts for hydrogen solubility within the thermodynamic equilibrium at the gas-liquid interface, competitive adsorption, and desorption of all components on/from the catalyst surface, and their corresponding catalytic surface reactions. Implementing a set of ordinary differential equations based on the proposed reaction network stated above, modelled concentrations and catalyst coverage values for each reaction constituent was calculated with the consideration of the following assumptions;

- 1) Based on the catalyst activity test with bare γ -alumina support (Fig. 6h) which resulted in negligible activity, as well as the verification of negligible metal leaching into the liquid phase, it is apparent that all reactions are heterogeneous in nature,
- 2) Based on catalyst activity tests with Ce-doped alumina (Figs. 7h and 8h) resulting in negligible activity, surface reactions are considered to be completely dependent on metallic sites,
- 3) H_2 undergoes dissociative adsorption on nickel metallic sites as is classically reported [73,74],
- 4) All related vacant sites for adsorption are considered equal and independent of the overall coverage,
- 5) Each active metallic site is covered by either one organic or hydrogen molecule at a time as they adsorb competitively on Ni sites,
- 6) Adsorption and desorption constants of products with analogous structures (i.e. saturated furan ring, unsaturated furan ring, and ring opened products) are considered equivalent,

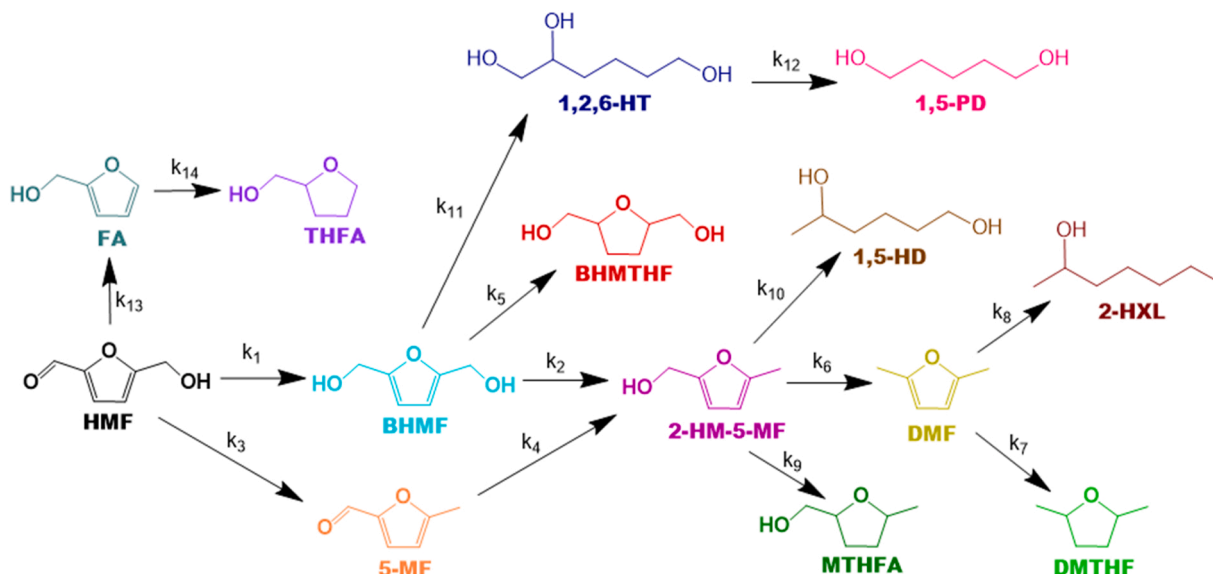


Fig. 5. Proposed detailed reaction network of HDO of HMF.

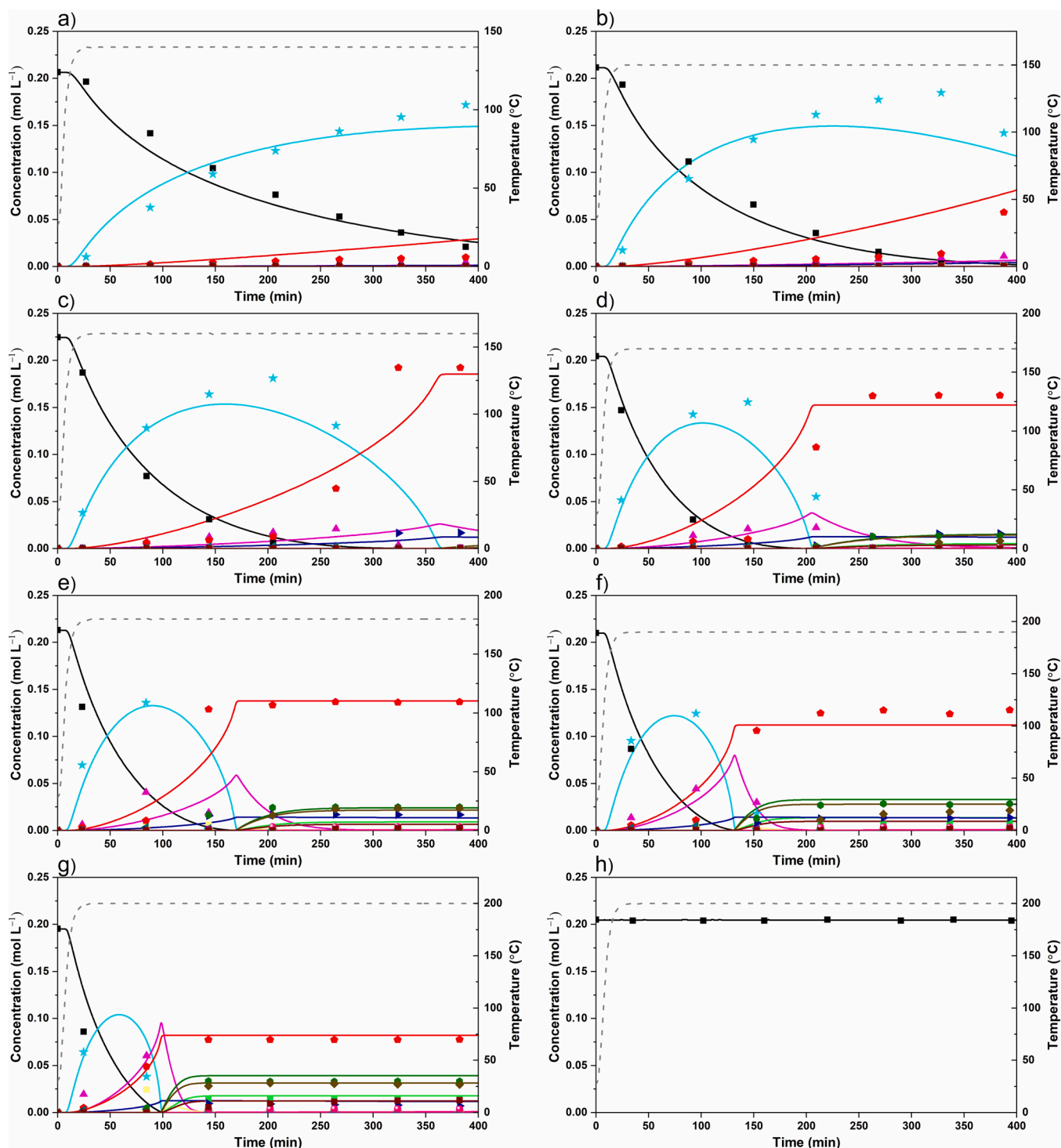


Fig. 6. Temperature influence on product distribution over time in pure THF using 10Ni/Al₂O₃ at a) 140 °C, b) 150 °C, c) 160 °C, d) 170 °C, e) 180 °C, f) 190 °C, g) 200 °C, and h) blank Al₂O₃ at 200 °C. ■ HMF, ★ BHMF, ▼ 5-MF, ▲ 2-HM-5-MF, ▼ DMF, ◆ BHMTHF, ▼ DMTHF, ▼ FA, ▼ THFA, ▼ 1,2,6-HT, ▼ 1,5-PD, ▼ MTHFA, ▼ 1,5-HD, ▼ 2-HXL. — — — Temperature. Lines correspond with modelled values whereas symbols correspond with experimental values.

7) Analogous to reports elsewhere, products containing a saturated furan ring (BHMTHF, DMTHF, MTHFA) were considered rapidly desorbed and do not react any further [68]. This was also validated when a subsequent activity test with a final mixture resulted in unaffected BHMTHF concentrations (Figure S.10b),

8) Hydrogen solubility in THF was linearized from previously reported Henry constant values to align to the implemented reaction conditions in this study (140 – 200 °C and 5 MPa of H₂) [75],
 9) As a result of the relatively high initial H₂ pressure of 5 MPa, concentrations of the additional (initially liquid) products in the gas phase were considered to be negligible and were not incorporated in the set of ordinary differential equations,

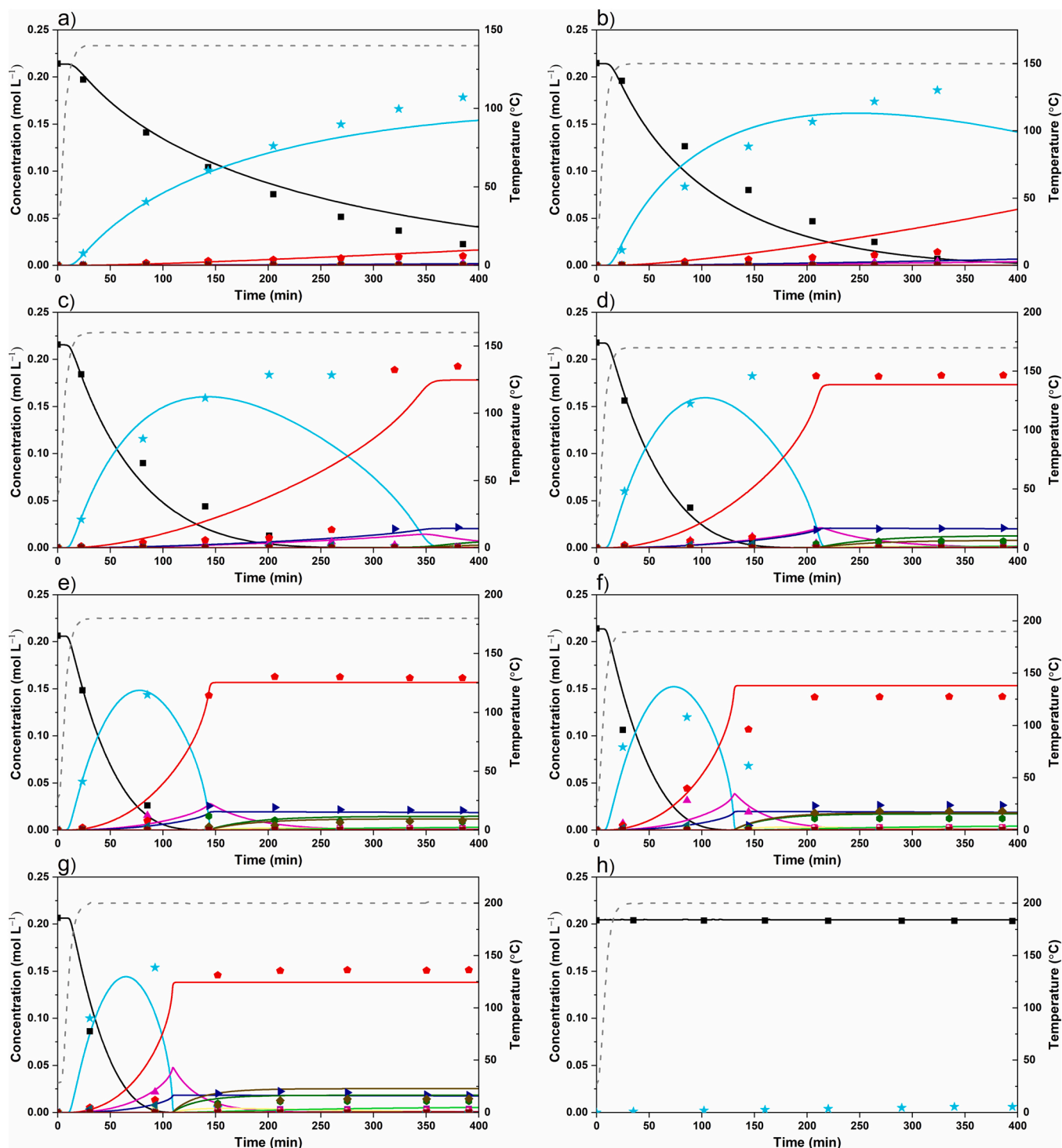


Fig. 7. Temperature influence on product distribution over time in pure THF using 10Ni15Ce/Al₂O₃ at a) 140 °C, b) 150 °C, c) 160 °C, d) 170 °C, e) 180 °C, f) 190 °C, g) 200 °C, and h) 15Ce/Al₂O₃ at 200 °C. ■ HMF, ★ BHMF, ▼ 5-MF, ▲ 2-HM-5-MF, ◆ DMF, ◆ BHMTHF, ◆ DMTHF, ◆ FA, ◆ THFA, ◆ 1,2,6-HT, ◆ 1,5-PD, ◆ MTHFA, ◆ 1,5-HD, ◆ 2-HXL. — — — Temperature. Lines correspond with modelled values whereas symbols correspond with experimental values.

10) Tests that included water as co-solvent were simply modelled by setting k_2 , k_3 , k_{12} , k_{13} to 0 and maintaining the same activation energies as when water was omitted from the reaction media.

Adsorption rate (r_j^{ads}) of each compound j depends on the adsorption rate constant (k_j^{ads}), its liquid phase concentration (C_j^{L}), and vacant site concentration (Θ_{VS}), defined in Eq.1.

$$r_j^{\text{ads}} = k_j^{\text{ads}} C_j^{\text{L}} \Theta_{\text{VS}} \quad (1)$$

Desorption rate (r_j^{des}) of each compound j depends on the desorption rate constant (k_j^{des}), and coverage of j adsorbed to active sites (Θ_j), defined in Eq.2.

$$r_j^{\text{des}} = k_j^{\text{des}} \Theta_j \quad (2)$$

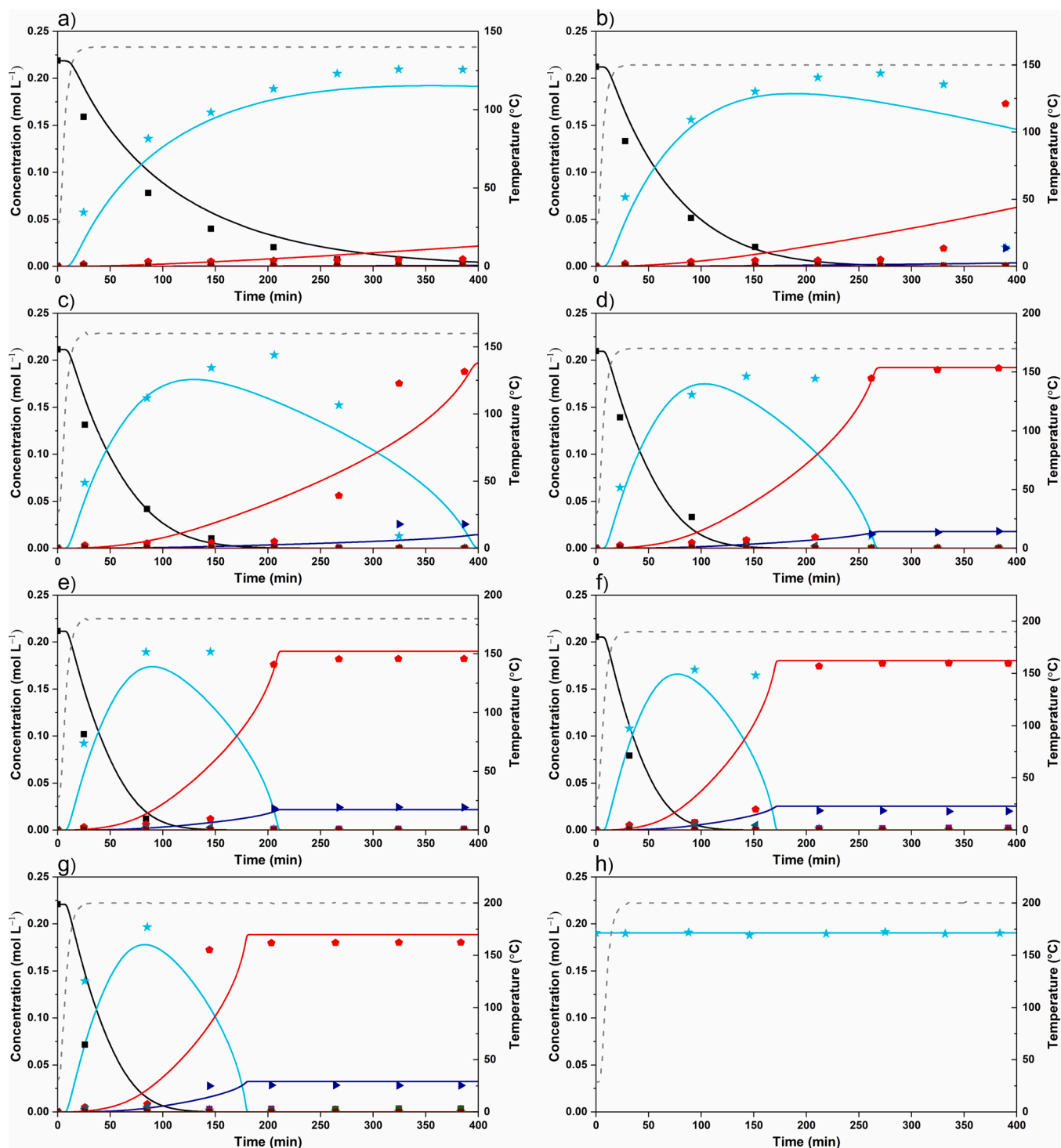


Fig. 8. Temperature influence on product distribution over time in 5 vol% H₂O and THF using 10Ni/Al₂O₃ at a) 140 °C, b) 150 °C, c) 160 °C, d) 170 °C, e) 180 °C, f) 190 °C, g) 200 °C, and h) starting from BHMF with 15Ce/Al₂O₃ at 200 °C. ■ HMF, ★ BHMF, ▲ 5-MF, ▲ 2-HM-5-MF, ■ DMF, ● BHMTHF, ■ DMTHF, ▲ FA, ■ THFA, ▲ 1,2,6-HT, ● 1,5-PD, ● MTHFA, ● 1,5-HD, ■ 2-HXL. — — — Temperature. Lines correspond with modelled values whereas symbols correspond with experimental values.

Surface reaction rate (r_i^{surf}) of each reaction i depends on the surface reaction rate constant (k_i^{surf}) and coverage of corresponding reactant j (Θ_j) and hydrogen (for hydrogenation reactions) adsorbed to active sites, defined in Eq. 3.

$$r_i^{surf} = k_i^{surf} \Theta_j \Theta_H \quad (3)$$

The kinetic model considers both the isothermal segment of the process at the final temperature and the initial heat ramping stage of the reaction mixture to the specified reaction temperature. Reaction temperatures and pressures were recorded during each experiment and implemented for each time step to calculate reaction rate constants, mass transfer constants, and thermodynamic properties such as equilibrium hydrogen solubility. Adsorption and desorption rate constants

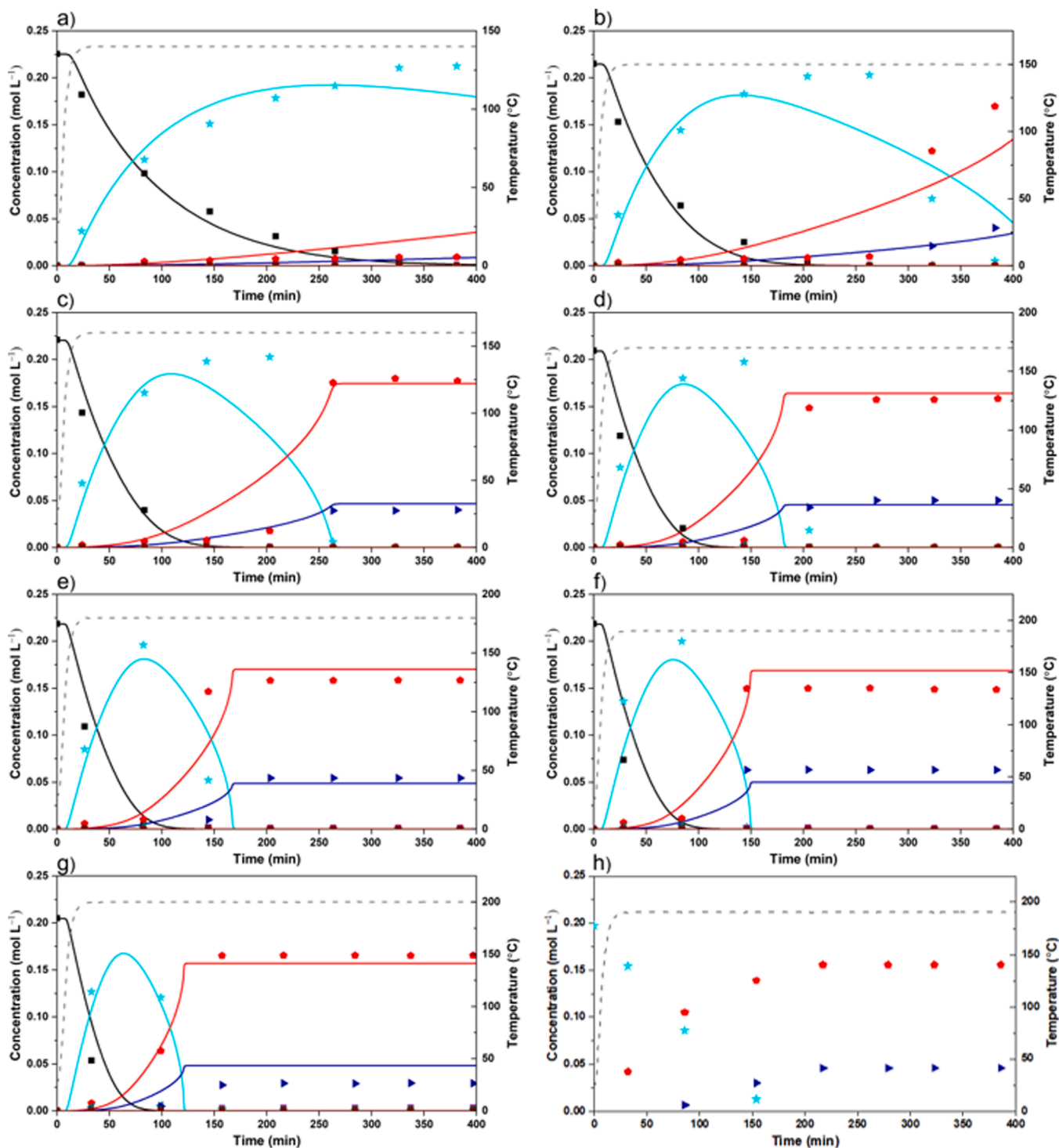


Fig. 9. Temperature influence on product distribution over time in 5 vol% H₂O and THF using 10Ni15Ce/Al₂O₃ at a) 140 °C, b) 150 °C, c) 160 °C, d) 170 °C, e) 180 °C, f) 190 °C, g) 200 °C, and h) starting from BHMf with 10Ni15Ce/Al₂O₃ at 190 °C. ■ HMF, ★ BHMf, ▲ 5-MF, ▲ 2-HM-5-MF, ■ DMF, ● BHMTHF, ■ DMTHF, ■ FA, ■ THFA, ▲ 1,2,6-HT, ● 1,5-PD, ■ MTHFA, ▲ 1,5-HD, ■ 2-HXL. — — Temperature. Lines correspond with modelled values whereas symbols correspond with experimental values.

were considered independent of temperature and orders of magnitude higher than the (comparatively low) reaction rate constants. The temperature influence on rate constants for surface reactions was employed to follow Arrhenius law as presented in Eq. 4;

$$k_i^{\text{surf}}(T_2) = k_i^{\text{surf}}(T_1) \times \exp\left(\frac{E_{a_i}}{R} \left(\frac{1}{T_1} - \frac{1}{T_2}\right)\right) \quad (4)$$

Differential balance equations based on the proposed reaction network (Eq. 6) and Eq. 1–3 were implemented as follows;

General balance for H₂ concentration $C_{\text{H}_2}^G$ in the headspace volume of

the reactor (V_G), where $k_{GL}a$ dependence on the stirring speed in this type of reactor was adopted from our previous work [76]:

$$\frac{dC_{H_2}^G}{dt} = -k_{GL}a \left(\frac{p_{H_2}}{H} - C_{H_2}^L \right) \frac{V_L}{V_G} \quad (5)$$

General balance for liquid phase, where n_{TS} is the surface concentration of metal sites and V is the volume of the liquid phase:

$$\frac{dC_j^L}{dt} = -r_j^{ads} + r_j^{des} \frac{n_{TS}}{V} \quad (6)$$

General balance for concentration of H_2 in liquid phase:

$$\frac{dC_{H_2}^L}{dt} = +k_{GL}a \left(\frac{p_{H_2}}{H} - C_{H_2}^L \right) - r_j^{ads} + r_j^{des} \frac{n_{TS}}{V} \quad (7)$$

General balance for coverage of active sites:

$$\frac{d\Theta_j}{dt} = r_j^{ads} \frac{V}{n_{TS}} + r_j^{des} + \sum_i \pm r_i^{surf} \quad (8)$$

For all the reactions i -s (I is their number) that consume or form j . The vacant active site coverage was balanced with the consideration of Eq. 8.

$$\frac{d\Theta_{vs}}{dt} = \sum_j r_j^{ads} \frac{V}{n_{TS}} + \sum_j r_j^{des} + \sum_i (\pm r_i^{surf}) \quad (9)$$

For all compounds j -s (J is their number) that adsorb/ desorb and for all reactions i -s (I is their number) that have unstoichiometric balance of sites. If the reactant-product molar ratio is always 1–1 or 2–2, then the last sum can be omitted.

A set of ordinary differential equation (ODE) solved with Runge-Kutta (2,3), based on the applied Matlab solver, were used to model concentration profiles. Initial concentrations of all components were set at 0, apart from the starting reactant (HMF) in the liquid phase, and the H_2 partial pressure in the gas phase (calculated by Henry law). To our understanding, the solubility of hydrogen in tetrahydrofuran has only been estimated by Brunner [75] which was applied in the calculation of Henry's constant in Eq. 10 and in Eq. 7, where H denotes Henry's constant defined via concentration, p_{H_2} is the partial pressure of hydrogen in the gas phase, and C_{H_2} relates to the concentration of hydrogen in the solvent. The phase-equilibrium offered by Brunner and the attained Henry's constant showed exponential dependence on temperature in the form of

$$H = 2544.132 \times e^{-0.007272 \cdot T} \quad (10)$$

The total concentration of active sites on the catalyst surface (Θ_{VS}) were determined independently by CO-TPD chemisorption (see Table 3).

$$f(k_{i-j}, Ea_{i-j}) = \sum (C_{exp} - C_{mod(k_{i-j}, Ea_{i-j})})^2 \quad (11)$$

Nelder–Mead method was implemented for coarse regression of the experiments with the same catalyst type simultaneously by minimization of the objective function (Eq. 11), whereas the Levenberg–Marquardt method was used for fine regression analysis and to calculate Jacobian matrix.

Turnover frequencies (TOF) for each distinct catalyst were calculated using the overall equation;

$$TOF = k_i^{surf} \Theta_i \Theta_H \quad (12)$$

Where a continual maximum temperature of 200 °C and corresponding initial concentrations of each reactant j were applied for optimal comparative purposes.

3.4. Catalytic activity tests and modelled results

Experimental (symbols) and modelled (lines) liquid phase concentrations as a function of time for reaction temperatures between 140 °C

and 200 °C are displayed in Figs. 6–9 and their corresponding kinetic parameters from the regression analysis are reported in Table 4.

When applying the 10Ni catalyst in pure THF, full conversion was reached after the entire reaction time once the reaction temperature was raised to 160 °C or greater. Below 160 °C, BHMTHF was the dominant product with small amounts of BHMTHF and 2-HM-5-MF. Aldehyde reduction towards alcohols is known to occur rather readily on Ni metallic sites, typically through a hydrogen attack to the O atom of the carbonyl group and stabilization of the hydroxyalkyl intermediate from the furan ring [77,78]. According to the reaction rate constants presented in Table 4, k_1 is undoubtedly the highest rate with $2.5 \cdot 10^3 \text{ min}^{-1}$, demonstrating that aldehyde reduction transpires very quickly. As previously mentioned, blank activity tests with bare Al_2O_3 (Fig. 6h) and Ce-doped support (Figs. 7h and 8h) that resulted in negligible activity confirmed that k_1 is highly dependent on the presence of metallic sites and cannot continue without them. As the reaction temperature increased to 160 °C, BHMTHF became the main product. It was not possible to break the C-O bond amid the saturated furan ring with our Ni-based catalysts. This outcome is rather contradictory to the fact that the C-O bond within DMF is reported to be 28 kJ/mol stronger in relation to the same bond in DMTHF [72]. This phenomenon suggests that the adsorbance of the unsaturated furan ring onto the catalyst surface is an essential part in weakening the C-O bond to facilitate easier bond breakage. Ring opened products also emerged when reaction temperatures increased above 170 °C which included 1,2,6-hexanetriol, 1, 5-hexanediol, as well as minute amounts of 2-hexanol at 200 °C. Traces of 1,5-pentadiol were also detected at elevated reaction temperatures above 170 °C. Once the reaction temperature was increased further to 180 °C and 190 °C, a significant amount of dehydrated products formed originating from 2-HM-5-MF with k_2 being $3.6 \cdot 10^1 \text{ min}^{-1}$. This initial dehydration reaction also was the lowest reaction rate constant amongst all subsequent reactions from k_6 to k_{10} , indicating that k_2 was the rate-limiting step towards any deoxygenated product. In the absence of water, ring saturation of dehydrated products yielding DMTHF and MTHFA (k_7 and k_9) was favoured over ring opening towards 2-HXL and 1,5-HD (k_8 and k_{10}) at elevated temperatures. This was similarly observed with the competing ring saturation (k_5) and ring opening (k_{11}) reactions of BHMTHF with reaction rate constants of $1.4 \cdot 10^2 \text{ min}^{-1}$ and $1.2 \cdot 10^1 \text{ min}^{-1}$, respectively. This behaviour aligns with what has been commonly described in which cleavage of the aromatic C-O bond amongst the furan ring typically has a higher activation energy relative to ring saturation [68,79].

The incorporation of Ce to the nickel-based catalyst changed product selectivity considerably, particularly at elevated temperatures. Similar to unpromoted Ni, aldehyde reduction yielding BHMTHF was the dominate reaction below 170 °C with trace amounts of BHMTHF, 2-HM-5-MF, and FA. Relative to 10Ni, k_1 slowed by over 50% to 932 min^{-1} , yet remained the highest reaction rate. Dehydration reactions were significantly lessened in the promoted 10Ni15Ce catalyst, as observed in the sudden drop of k_2 from $3.6 \cdot 10^1 \text{ min}^{-1}$ to 5.4 min^{-1} , and k_6 from $2.8 \cdot 10^1 \text{ min}^{-1}$ to 3.2 min^{-1} . Ring saturation of 2-HM-5-MF towards MTHFA remained favored over ring opening. Only once the reaction temperature reached ≥ 160 °C was it possible to achieve sufficient amounts of ring saturation and ring opened products, namely BHMTHF and 1,2,6-HT, respectively. Compared to the 10Ni catalyst, BHMTHF selectivity was generally improved at higher temperatures ≥ 180 °C. Ceria addition also enhanced 1,2,6-HT selectivity moderately to a maximum of 12% at 190 °C. However, despite these improvements to ring opening and ring saturation, both k_5 and k_{11} were exceptionally stalled by over 300% to $4.0 \cdot 10^1 \text{ min}^{-1}$ and 4.8 min^{-1} in comparison to the 10Ni catalyst, respectively. In fact, doping the catalyst with ceria lead to a substantial decrease in TOF for essentially every reaction compared to the unpromoted Ni catalyst, as clearly shown in Table 4. This overall waning in reaction rate constants and TOFs, particularly with k_1 , appears rather contrary to H_2 -TPR and CO-TPD analysis that indicated that doping with ceria improved reducibility and increased vacant metallic sites,

Table 4

Kinetic parameters and TOF for the hydrotreatment of HMF over Ni-based alumina catalysts.

i	Reaction rate constants at XXX °C (k_i), min ⁻¹				Activation energies (E_{a_i}), KJ mol ⁻¹				Turnover Frequencies (TOF) at 200 °C, min ⁻¹			
	10Ni	10Ni (H ₂ O)	10Ni15Ce	10Ni15Ce (H ₂ O)	10Ni	10Ni (H ₂ O)	10Ni15Ce	10Ni15Ce (H ₂ O)	10Ni	10Ni (H ₂ O)	10Ni15Ce	10Ni15Ce (H ₂ O)
1	2.5·10 ³	7.1·10 ³	9.3·10 ²	5.2·10 ³	139	139	168	168	209	501	34.1	460
2	3.6·10 ¹	0	5.4	0	230	n.a.	220	n.a.	6.67	0	0.32	0
3	0	0	0	0	n.a.	n.a.	n.a.	n.a.	0	0	0	0
4	0	0	0	0	n.a.	n.a.	n.a.	n.a.	0	0	0	0
5	1.4·10 ²	1.0·10 ²	4.0·10 ¹	8.4·10 ¹	139	139	164	164	25.3	19.2	3.16	18.8
6	2.8·10 ¹	0	3.2	0	152	n.a.	64.6	n.a.	0.24	< 0.01	0.03	< 0.01
7	9.8·10 ¹	0	6.7·10 ⁻¹	0	26.7	n.a.	10.1	n.a.	0.37	< 0.01	0.01	< 0.01
8	7.3·10 ¹	0	6.3·10 ⁻²	0	22.2	n.a.	22.5	n.a.	0.28	< 0.01	< 0.01	< 0.01
9	4.7·10 ¹	0	1.5·10 ¹	0	137	n.a.	32.8	n.a.	0.40	< 0.01	0.16	< 0.01
10	4.5·10 ¹	0	9.1	0	127	n.a.	79.9	n.a.	0.38	< 0.01	0.08	< 0.01
11	1.2·10 ¹	9.4	4.8	2.3·10 ¹	176	176	16.9	16.9	2.12	1.78	0.37	5.21
12	1.1·10 ⁻¹	0	1.4·10 ⁻¹	0	12.0	n.a.	11.6	n.a.	< 0.01	0	< 0.01	0
13	2.1·10 ⁻²	0	< 1.4·10 ⁻²	0	10.1	n.a.	35.8	n.a.	< 0.01	0	< 0.01	0
14	2.3·10 ⁻²	0	2.2·10 ⁻²	0	16.8	n.a.	16.2	n.a.	< 0.01	< 0.01	< 0.01	< 0.01

respectively. Similar studies have suggested that HMF hydrogenation requires the synergistic effect of both metallic (Ni⁰) and electrophilic (Ni²⁺) species, in which Ni²⁺ is initially involved in the adsorption and activation via the oxygen amongst the carbonyl group, and Ni⁰ provides the dissociated hydrogen to attack the polarized C atom [80–82]. Others have reported that Lewis acid sites provided by the support can also facilitate in polarization and activation of the C=O bond in the same way [19,83]. Thus, the loss in hydrogenation activity of HMF that was observed following ceria promotion may be the result of both, i) the alteration in the proportion of Ni⁰/Ni²⁺ species on the catalyst surface, and ii) the significant decrease in acid sites which was determined during NH₃-TPD. Additionally, the loss in acidity can also clarify the other lower reaction rate constants corresponding to dehydration products as acid sites have been commonly recognized to facilitate dehydration [84–86]. On the other hand, improved reducibility of Ni species that was observed after the incorporation of Ce allows hydrogen-demanding reactions such as ring saturation and ring opening to occur much more readily, hence the improvements in BHMTHF and 1, 2,6-HT yields that occurred.

Both catalysts were then subjected to analogous activity tests but with replacing 5 vol% of THF with water. As shown in Figs. 8 and 9, the addition of water as a co-solvent stopped essentially all dehydration reactions for both catalysts, enabling BHMTHF and 1,2,6-HT to be nearly the only products. Substituting 5 vol% of THF with H₂O also considerably enhanced k_1 from 2.5·10³ min⁻¹ to 7.1·10³ min⁻¹ for the 10Ni catalysts, and from 9.3·10² min⁻¹ to 5.2·10³ min⁻¹ for the 10Ni15Ce catalyst. Although water addition resulted in unanimously stopping dehydration reactions across all reaction temperatures, the concluding impact on reaction rate constants and TOF for ring saturation (k_5) and ring opening (k_{11}) were opposing for each catalyst. For example, 5 vol% water amplified TOFs for both ring saturation and ring opening reactions by over 500% for the 10Ni15Ce catalyst, however, were slightly decreased in regards to the unpromoted 10Ni catalyst, as shown in Table 4. Furthermore, BHMTHF formation occurred much more readily for the 10Ni catalyst compared to when employing only pure THF, even achieving the maximum in this study of 91% selectivity at 170 °C. Sizable amounts of BHMTHF were also achieved at a lower temperature (150 °C) for both catalysts within the allotted reaction time. This likely relates to the substantial increase in k_1 that was observed as some studies have reported that the adsorbance of the aldehyde group amongst HMF out competes the adsorbance of the furan ring on the catalyst surface [87,88]. Therefore, as clearly seen in Figs. 6–9, only once HMF is nearly fully converted and relatively absent on the surface of the catalyst can BHMTHF consequently adsorb and react further. Contrarily, ring opening yielding 1,2,6-HT was much more prevalent with the 10Ni15Ce catalyst relative to the 10Ni catalyst in the presence of water, reaching a maximum selectivity of 26% compared to

only around 13% for the latter. Several publications have reported that the facilitator in either ring opening or ring saturation of BHMTHF is dependent on its adsorption configuration in either a tilted or parallel orientation, respectively [17,89,90]. Although, no study has been able to conclusively identify which type of active site(s) encourage each adsorption configuration. At first glance, the results from Table 3 suggest that a catalyst with a higher ratio of acidic to basic sites (5.1 versus 2.5 for 10Ni and 10Ni15Ce 400 Å, respectively) is more prone towards ring saturation to BHMTHF rather than ring opening to 1,2,6-HT when water is applied as a co-solvent. Subsequently, H₂O-TPD-MS was performed to determine if water adsorption differed between catalysts (Figure S.11). Two main peaks can be observed where the first broad signal ranges between 100–400 °C and a second sharp peak centered at 494 °C. The H₂O-TPD spectra demonstrate that the promoted 10Ni15Ce catalyst adsorbs noticeably more water relative to the 10Ni catalyst, but it was initially not clear on how the water adsorbed to the catalyst. To better understand the influence water had on acidic and/or basic sites, the catalysts were subjected to supplementary CO₂ and NH₃-TPDs following a preliminary water adsorption step with desorption up to 190 °C (relevant reaction temperature), as shown in Figure S.12 and S.13, respectively. As indicated in both CO₂ and NH₃-TPDs, an initial water adsorption step resulted in a significant decrease in both acid and basic sites, specifically decreasing those that are stronger in strength (> 200 °C). The blocking or filling of these specific active sites by water molecules is expected to prevent or alter the adsorption of certain functional groups, similar to what has been reported elsewhere [25,91, 92].

3.5. Influence of Ceria Pretreatment on Product Selectivity

Activity tests using different pretreated 10Ni15Ce catalysts were then carried out to investigate and better understand the subtle influence oxygen vacancies and ensuing fluctuations in acidic and basic sites have on product selectivity. The product selectivity distribution following 6 h activity tests at 190 °C are displayed in Fig. 10 in pure THF (a) and 5 vol% H₂O:THF (b) solvent systems. All omitted selectivity is BHMTHF, which was not presented for superior comparative purposes. When pure THF was used as solvent, the prevalence of all dehydration products were as followed; 800 Å (13%) ≈ 800 N (12%) > 400 N (10%) > 400 Å (4%). Initially, this trend would suggest that deoxygenation is facilitated by the presence of oxygen vacancies, possibly acting as adsorption sites for the O atom amid the alcohol groups, similar to what has been reported elsewhere [26,28,93]. However, as indicated in Figure S.14(i), the trend is rather mediocre ($R^2 = 0.81$), and is contradictory when equating the promoted catalysts to the 10Ni catalyst that resulted in the highest amount of dehydration products (17%). Thus, the prevalence of dehydration appears to be predominately due to the

increased acidity of the catalyst, yet oxygen vacancies must also independently aid in facilitating dehydration as has been similarly described elsewhere [94,95]. Furthermore, neither ring opening nor ring saturation seem to follow the pattern of oxygen vacancies when water is omitted. Instead, there appears to be an obvious inclination between higher total acidity of the catalyst and less ring saturation products ($R^2 = 0.94$), along with higher total acidity and more ring opened products ($R^2 = 0.96$), as shown in Figure S.14(ii) and S.14(iii), respectively. This would imply that both of these reactions are highly dependent on acid sites, although it is problematic to identify specifically which strength of acid site is relevant since all the catalysts demonstrated equivalent acid site strength distribution in NH_3 -TPD analysis (Fig. 4a). Since NH_3 -TPDs after H_2O adsorption demonstrated a loss of strong acidic sites, this possibly indicates that either these stronger Lewis acid sites, or a catalyst with strong acidic surface, could allow the electron-dense furan ring to be in closer proximity to the catalyst surface to adsorb in a parallel configuration, allowing ring saturation to occur more readily. On the other hand, weaker acidic sites, or a weaker acidic catalyst surface, could allow BHMF to adsorb more distantly in a tilted configuration, facilitating ring opening. Furthermore, the influence of oxygen vacancies as strong basic sites does not seem to supersede the impact that acidic sites have on the 1,2,6-HT yields since both 800 A and 800 N catalysts are more comparable to the 10Ni catalyst (containing minimum oxygen vacancies) rather than the 10Ni15Ce 400 A catalyst.

Next, the pretreated promoted NiCe catalysts were subjected to similar activity tests with the replacement of 5 vol% H_2O , and likewise, nearly all dehydration products were hindered except for ~1% for both 800 A and 800 N catalysts. Additionally, minor amounts of BHMF were also detected for both 800 A and 800 N catalysts, probably due to the moderate decrease in surface area and small pores that was occurred when pretreating at higher temperatures (Table 2). H_2O -TPD spectra of the 10Ni15Ce 800 N catalyst indicated that water adsorption appears to increase with the expected number of oxygen vacancies in comparison with the 10Ni and 10Ni15Ce 400 A catalysts (Figure S.11). This also correlates with CO_2 -TPD results following the initial water adsorption (Figure S.12) in which oxygen vacancies were effectively obstructed by adsorbed water molecules. This aligns with other studies that report that oxygen vacancies act as “hot-spots” that water is more likely to bind to [96–98]. After water was added as a co-solvent, 1,2,6-HT selectivity for the promoted 10Ni15Ce catalysts were as followed; 400 A (26%) > 400 N (19%) > 800 A (10%) \approx 800 N (9%). When comparing to the 10Ni catalyst with a 1,2,6-HT selectivity of 9%, ring opening towards 1,

2,6-HT assumes to be associated with the prevalence of basic sites in the presence of water rather than acid sites which was observed when water was absent (Figure S.14(iv)). For example, it was determined that 10Ni15Ce 400 A and 10Ni15Ce 800 N catalysts contained relatively equal number of acidic sites when water was added to the system ($217 \mu\text{mol g}^{-1}$ and $220 \mu\text{mol g}^{-1}$, respectively), however, 1,2,6-HT selectivity was nearly three times higher with the former. This change in trend could be caused by water blocking stronger acidic sites, permitting basic sites to be more accessible and their impact on product selectivity more prominent (Figure S.13). As described above, CO_2 -TPD results indicated these basic sites are predominately hydroxyl groups on the surface of the catalyst (Fig. 4b). It has been recognized that water can direct themselves onto coordinatively, unsaturated Al species and undergo hydrogen bonding with these surface hydroxyls [99–101]. Therefore, it is proposed that water molecules could hydrogen bond to these surface hydroxyls, aiding in ring opening of BHMF. This could either occur by stabilizing intermediates long enough to allow C-O bond to be more readily cleaved, or they may allow proton-shuttling during hydrogenation reactions that has been described elsewhere [102,103]. Since 1,2,6-HT selectivity declines with extra oxygen vacancies amongst the 10Ni15Ce catalysts, it would appear that some water is being redirected to the oxygen vacancies rather than binding with the exposed surface hydroxyls, limiting the ability to induce ring opening.

3.6. Catalyst Recyclability and Stability

Recyclability tests of 10Ni and 10Ni15Ce 400 A catalysts with corresponding product yields are presented in Fig. 11 where the number of cycles is labelled as R1-R3. XRF analysis of the liquid phase demonstrated negligible Ni or Ce leaching (below the detection limit of 0.01 wt %). Detailed TEM analysis of spent 10Ni15Ce catalysts (Figure S.6) did not demonstrate any major difference in morphology when compared to reduced catalysts (Figure S.5, right column) where CeO_2 nanocrystals remained around 10 nm and were uniformly decorated across the alumina support. On some thin areas, some 1 nm size Ni nanoparticles (confirmed by EDXS analysis) are visible (Figure S.6 (a) and (c)) which could have been formed from the growth of Ni species during the catalytic tests. XRD spectra of spent 10Ni and 10Ni15Ce catalysts indicated negligible changes in diffraction peaks corresponding to CeO_2 and alumina where Ni remained undetectable following activity tests (Figure S.16). Generally, conversion remained consistently above 90% for 3 cycles of recycled tests for both 10Ni and 10Ni15Ce catalysts in

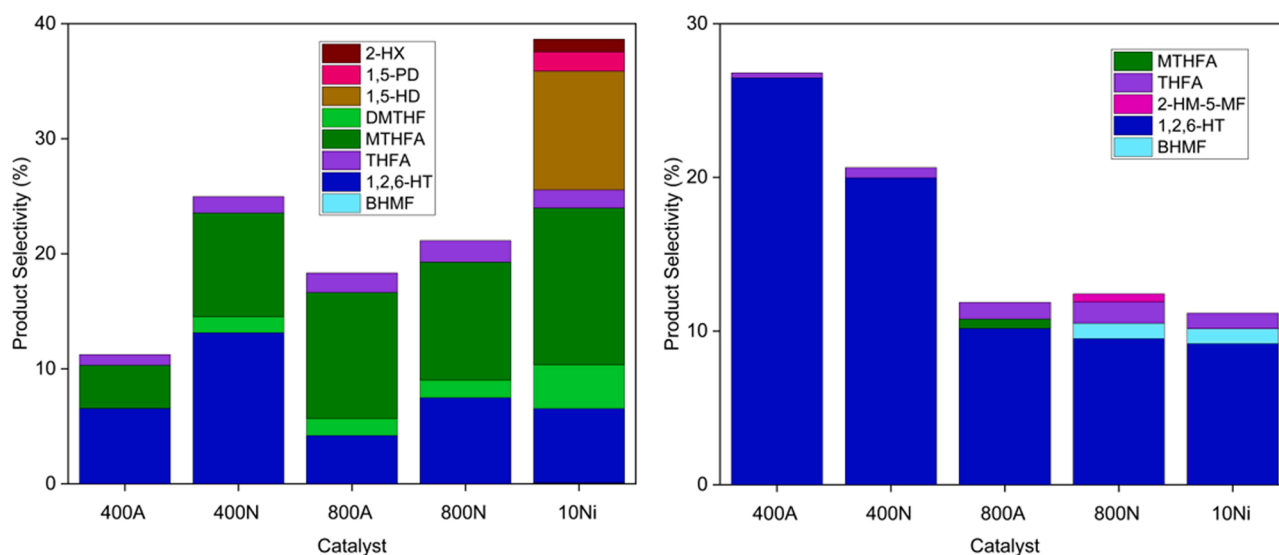


Fig. 10. Activity tests with different pretreated 10Ni15Ce and 10Ni catalysts in both pure THF (left) and 5 vol% H_2O in THF (right). (Reaction conditions: 190 °C, 50 bar of H_2 , 6 h). Remaining product selectivity not shown is BHMTF.

either solvent system, however, product selectivity altered significantly after the initial reaction. 10Ni15Ce catalyst in either pure THF (Fig. 11A) or water: THF (Fig. 11B) resulted in 1,2,6-HT and BHMTHF production being almost entirely restricted following the initial test, leaving BHMF as the main product. Regarding the 10Ni catalyst, it was able to maintain BHMTHF formation for a single recycled test in the absence of water (Fig. 11C) before succumbing to similar loss of ring saturation/opening capability whereas in the presence of water (Fig. 11D), BHMTHF selectivity was lost immediately. The cause for the drastic fluctuation in product selectivity could be either due to trace amounts of unconverted HMF inhibiting the adsorption and further conversion of BHMF as mentioned previously, or due to changes to the acido-basic properties of the catalyst, or a combination of both. It was generally observed that sites responsible for dehydration and decarbonylation reactions seemed to stay intact during recycled tests for both catalysts. NH_3 and CO_2 -TPD analysis of the spent catalysts detected substantial fluctuations on the surface of the catalyst compared to before activity tests, as shown in Figure S.15 and Figure S.16. Noteworthy was the emergence of very strong basic sites ($>400^\circ\text{C}$) that were not present prior to activity tests for both 10Ni15Ce 400 A and 10Ni catalysts in either solvent system. The presence of strong basic sites (O^{2-}) and slight loss of strong acid sites (mostly Al^{3+}) would significantly change the catalyst surface to be more negatively charged. Therefore, the failure in

enabling ring opening/ saturation reactions amongst the recycled tests is likely due to a repulsive effect on the furan ring, inhibiting it from adsorbing adequately. These recyclability results also validate the fact that aldehyde reduction yielding BHMF, dehydration, and decarbonylation reactions all likely occur solely on exposed Ni metallic sites and do not require active sites provided by alumina. Attempts at regenerating either catalyst via calcination was unsuccessful, even impeding conversion by 50% in the case of the 10Ni catalyst in water: THF (Fig. 11D). These conclusions suggest that the catalyst deactivation was not because of adsorbed carbon or organic species on the catalyst surface as others have reported with similar nickel-based catalysts [104,105]. Therefore, the modification of the surface properties of the catalyst (emergence of strong basic sites) and subsequent loss of activity is likely due to Ni species partially diffusing into the alumina lattice and/or the migration of Al species to the surface during consecutive reductions (and calcination) that was further exacerbated when exposed to hydrothermal reaction conditions [106,107]. This also correlates well with CO -TPD results of the spent catalysts that showed metallic sites began waning after the initial activity test (Table S.2). Additionally, XPS analysis indicated similar losses in surface Ni composition amongst the spent 10Ni and 10Ni15Ce catalysts compared to before activity tests, especially in the presence of water (Figure S.18 and Table S.2). Although NiAl_2O_4 spinels were not observed in the XRD spectra of the spent

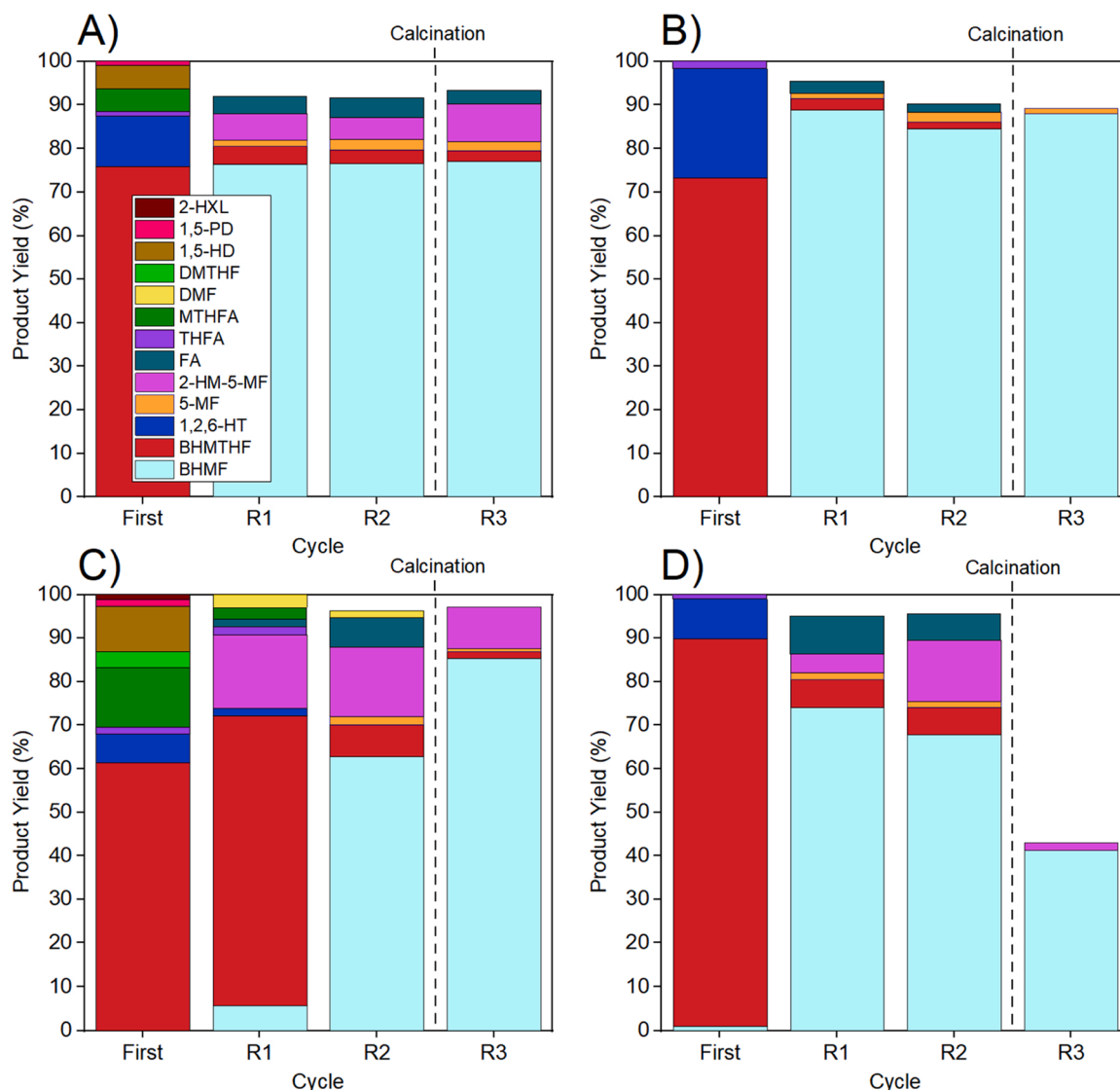


Fig. 11. Recyclability tests of A) 10Ni15Ce 400 A in pure THF, B) 10Ni15Ce 400 A in 5 vol% water: THF, C) 10Ni in pure THF, and D) 10Ni in 5 vol% water: THF.

catalysts (Figure S.17), their formation is also probable but are likewise under the detectable limit (< 4 nm).

4. Conclusions

This work synthesized ceria-promoted nickel-based catalysts supported on alumina and tested their catalytic activity for the hydrogenation of 5-hydroxymethylfurfural to value-added diols and triols where an extensive reaction network is presented based on catalytic activity tests. A kinetic model is also offered based on the proposed reaction pathway that takes into account thermodynamic effects, adsorption and desorption kinetics onto active sites, and mass transfer between gas and liquid phases. Applying ceria as a promoter to the Ni/Al₂O₃ catalyst resulted in diminishing the total number of acid sites and enhancing the total number of basic sites compared to the 10Ni catalyst. This modification to the acid-base properties of the catalyst lead to an improvement in both ring saturation yielding BHMTHF, and ring opening towards 1,2,6-hexanetriol. This was actually contrary to the decline in k_5 and k_{11} as well as TOFs that was reported in the 10Ni15Ce catalyst relative to unpromoted 10Ni. Subsequently, dehydration reactions were hampered in the 10Ni15Ce catalyst with significant dips in both k_2 and k_6 that were observed. Replacing 5 vol% of the THF with water proved to block a substantial portion of acidic and basic sites resulting in the elimination of unwanted dehydration reactions, allowing BHMTHF and 1,2,6-HT to be essentially the sole products. H₂O-TPDs demonstrated that water adsorbs onto the catalyst predominantly onto oxygen vacancies. NH₃-TPDs after an initial H₂O adsorption step further indicated that strong acidic sites are blocked by adsorbed water. Thus, it is hypothesized that a stronger acidic catalyst surface facilitates the parallel adsorption of the furan ring to permit ring saturation, whereas a surface with weaker acidity promotes a tilted adsorption configuration to allow ring opening to transpire. Pretreating ceria under different conditions following the initial impregnation of the promoted 10Ni15Ce catalysts caused noteworthy changes to the surface properties of the catalyst, particularly by inducing oxygen vacancy formation. In the absence of water, 10Ni15Ce catalysts with higher oxygen vacancy content led to an increase in dehydration products. Although, when comparing to the 10Ni catalyst, dehydration seems to be predominately due to the presence of acidic sites, but is likely further promoted in the presence of oxygen vacancies. The improvements to 1,2,6-hexanetriol yields when water was added correlated with the increased basic sites amongst the promoted 10Ni15Ce catalysts, specifically those related to surface hydroxyls. Both the 10Ni and 10Ni15Ce 400 Å catalysts maintained nearly full conversion of HMF after several recycled tests, however, the ability to carry out either ring saturation or ring opening reactions was promptly lost, especially in the presence of water. This was expected to be the result of partial diffusion of nickel into the alumina lattice or alumina migration to the surface after successive reductions (and calcination) which was worsened under hydrothermal conditions. Overall, modelled values fit experimental results reasonably well, contributing valuable information to a deepened understanding of the complex factors relevant for HMF hydrogenation and more effective catalyst design. Future work will broaden the presented kinetic model to better comprehend the deciding causes between ring saturation and ring opening reactions.

CRedit authorship contribution statement

Brett Pomeroy: Writing-original draft preparation, conceptualization, methodology. Miha Grilc: Project administration, writing-review & editing. Sašo Gyergyek: Investigation, validation. Blaž Likozar: Resources, supervision, funding acquisition.

Declaration of Competing Interest

The authors declare the following financial interests/personal relationships which may be considered as potential competing interests:

Blaz Likozar reports financial support was provided by EU Framework Programme for Research and Innovation Leadership in Enabling and Industrial Technologies. Blaz Likozar reports financial support was provided by Public Research Agency of the Republic of Slovenia. Miha Grilc reports financial support was provided by Public Research Agency of the Republic of Slovenia. Blaz Likozar has patent #PCT/EP2022/059475 pending to National Institute of Chemistry, Slovenia. Miha Grilc has patent #PCT/EP2022/059475 pending to National Institute of Chemistry, Slovenia. Brett Pomeroy has patent #PCT/EP2022/059475 pending to National Institute of Chemistry, Slovenia.

Data Availability

Data will be made available on request.

Acknowledgements

The authors would like to acknowledge the financial support of by the EU Framework Program for Research and Innovation Horizon 2020 under Grant agreement no. 814416 (Reaxpro) and the ARRS (Program P2-0152 and postdoctoral research project Z2-9200). Mr. Jošt Mohorko servility is also acknowledged for his excellent and rapid XRF elemental analysis.

Appendix A. Supporting information

Supplementary data associated with this article can be found in the online version at doi:10.1016/j.apcatb.2023.122868.

References

- [1] X. Tang, J. Wei, N. Ding, Y. Sun, X. Zeng, L. Hu, S. Liu, T. Lei, L. Lin, Chemoselective hydrogenation of biomass derived 5-hydroxymethylfurfural to diols: key intermediates for sustainable chemicals, materials and fuels, *Renew. Sustain. Energy Rev.* 77 (2017) 287–296, <https://doi.org/10.1016/j.rser.2017.04.013>.
- [2] R.J. Van Putten, J.C. Van Der Waal, E. De Jong, C.B. Rasrendra, H.J. Heeres, J.G. De Vries, Hydroxymethylfurfural, a versatile platform chemical made from renewable resources, *Chem. Rev.* 113 (2013) 1499–1597, <https://doi.org/10.1021/cr300182k>.
- [3] J. He, S.P. Burt, M. Ball, D. Zhao, I. Hermans, J.A. Dumesic, G.W. Huber, Synthesis of 1,6-Hexanediol from Cellulose Derived Tetrahydrofuran-Dimethanol with Pt-WO_x/TiO₂ Catalysts, *ACS Catal.* 8 (2018) 1427–1439, <https://doi.org/10.1021/acscatal.7b03593>.
- [4] G.M. Mullen, E.J. Evans, B.C. Siegart, N.R. Miller, B.K. Rosselet, I. Sabzevari, A. Brush, Z. Duan, C. Buddie Mullins, The interplay between ceria particle size, reducibility, and ethanol oxidation activity of ceria-supported gold catalysts, *React. Chem. Eng.* 3 (2018) 75–85, <https://doi.org/10.1039/c7re00175d>.
- [5] X. Liao, Y. Liu, W. Chu, S. Sall, C. Petit, V. Pitchon, V. Caps, Promoting effect of AuCu alloying on Au-Cu/CeO₂-catalyzed CO oxidation: a combined kinetic and in situ DRIFTS study, *J. Catal.* 382 (2020) 329–338, <https://doi.org/10.1016/j.jcat.2019.12.029>.
- [6] C. Papadopoulos, K. Kappis, J. Papavasiliou, J. Vakros, M. Kuśmierz, W. Gac, Y. Georgiou, Y. Deligiannakis, G. Avgoiropoulos, Copper-promoted ceria catalysts for CO oxidation reaction, *Catal. Today* 355 (2019) 647–653, <https://doi.org/10.1016/j.cattod.2019.06.078>.
- [7] Z. Zhang, Y. Wang, J. Lu, M. Wang, J. Zhang, X. Liu, F. Wang, Synthesis of 1,3-diols from isobutene and HCHO via Prins condensation-hydrolysis using CeO₂ catalysts: effects of crystal plane and oxygen vacancy, *Inorganics* 5 (2017) 1–11, <https://doi.org/10.3390/inorganics5040075>.
- [8] N. Miletić, U. Izquierdo, I. Obregón, K. Bizkarra, I. Agirrezabal-Telleria, L. V. Barrio, P.L. Arias, Oxidative steam reforming of methane over nickel catalysts supported on Al₂O₃-CeO₂-La₂O₃, *Catal. Sci. Technol.* 5 (2015) 1704–1715, <https://doi.org/10.1039/c4cy01438c>.
- [9] L. Yang, L. Pastor-Pérez, S. Gu, A. Sepúlveda-Escribano, T.R. Reina, Highly efficient Ni/CeO₂-Al₂O₃ catalysts for CO₂ upgrading via reverse water-gas shift: Effect of selected transition metal promoters, *Appl. Catal. B Environ.* 232 (2018) 464–471, <https://doi.org/10.1016/j.apcatb.2018.03.091>.
- [10] A. Iriondo, V.L. Barrio, J.F. Cambra, P.L. Arias, M.B. Guemez, M.C. Sanchez-Sanchez, R.M. Navarro, J.L.G. Fierro, Glycerol steam reforming over Ni catalysts supported on ceria and ceria-promoted alumina, *Int. J. Hydrog. Energy* 35 (2010) 11622–11633, <https://doi.org/10.1016/j.ijhydene.2010.05.105>.
- [11] M.S. Gyngazova, L. Negahdar, L.C. Blumenthal, R. Palkovits, Experimental and kinetic analysis of the liquid phase hydrodeoxygenation of 5-hydroxymethylfurfural to 2,5-dimethylfuran over carbon-supported nickel catalysts, *Chem. Eng. Sci.* 173 (2017) 455–464, <https://doi.org/10.1016/j.ces.2017.07.045>.

- [12] Y. Liu, M.A. Mellmer, D.M. Alonso, J.A. Dumesic, Effects of water on the copper-catalyzed conversion of hydroxymethylfurfural in tetrahydrofuran, *ChemSusChem* 8 (2015) 3983–3986, <https://doi.org/10.1002/cssc.201501122>.
- [13] B. Pomeroy, M. Grilc, S. Gyergyek, B. Likozar, Catalyst structure-based hydroxymethylfurfural (HMF) hydrogenation mechanisms, activity and selectivity over Ni, *Chem. Eng. J.* (2020), 127553, <https://doi.org/10.1016/j.cej.2020.127553>.
- [14] K.T.V. Rao, Y. Hu, Z. Yuan, Y. Zhang, C.C. Xu, Green synthesis of heterogeneous copper-alumina catalyst for selective hydrogenation of pure and biomass-derived 5-hydroxymethylfurfural to 2,5-bis(hydroxymethyl)furan, *Appl. Catal. A Gen.* 609 (2021), <https://doi.org/10.1016/j.apcata.2020.117892>.
- [15] J.J. Wiesfeld, M. Kim, K. Nakajima, E.J.M. Hensen, Selective hydrogenation of 5-hydroxymethylfurfural and its acetal with 1,3-propanediol to 2,5-bis(hydroxymethyl)furan using supported rhenium-promoted nickel catalysts in water, *Green. Chem.* 22 (2020) 1229–1238, <https://doi.org/10.1039/c9gc03856f>.
- [16] J. Ohyama, A. Esaki, Y. Yamamoto, S. Arai, A. Satsuma, Selective hydrogenation of 2-hydroxymethyl-5-furfural to 2,5-bis(hydroxymethyl)furan over gold sub-nano clusters, *RSC Adv.* 3 (2013) 1033–1036, <https://doi.org/10.1039/c2ra22190j>.
- [17] S. Fulignati, C. Antonetti, D. Licursi, M. Pieraccioni, E. Wilbers, H.J. Heeres, A.M. Raspolli Galletti, Insight into the hydrogenation of pure and crude HMF to furan diols using Ru/C as catalyst, *Appl. Catal. A Gen.* 578 (2019) 122–133, <https://doi.org/10.1016/j.apcata.2019.04.007>.
- [18] R. Alamillo, M. Tucker, M. Chia, Y. Pagán-Torres, J. Dumesic, The selective hydrogenation of biomass-derived 5-hydroxymethylfurfural using heterogeneous catalysts, *Green. Chem.* 14 (2012) 1413–1419, <https://doi.org/10.1039/c2gc35039d>.
- [19] X. Kong, R. Zheng, Y. Zhu, G. Ding, Y. Zhu, Y.W. Li, Rational design of Ni-based catalysts derived from hydrotalcite for selective hydrogenation of 5-hydroxymethylfurfural, *Green. Chem.* 17 (2015) 2504–2514, <https://doi.org/10.1039/c5gc00062a>.
- [20] X. Kong, Y. Zhu, H. Zheng, F. Dong, Y. Zhu, Y.W. Li, Switchable synthesis of 2,5-dimethylfuran and 2,5-dihydroxymethyltetrahydrofuran from 5-hydroxymethylfurfural over Raney Ni catalyst, *RSC Adv.* 4 (2014) 60467–60472, <https://doi.org/10.1039/c4ra09550b>.
- [21] Y. Zhang, A. Rezayan, K. Wang, J. Wang, C.C. Xu, R. Nie, On-demand, highly tunable, and selective 5-hydroxymethylfurfural hydrogenation to furan diols enabled by Ni and Ni₃Ga alloy catalysts, *ACS Catal.* 13 (2023) 803–814, <https://doi.org/10.1021/acscatal.2c05451>.
- [22] H. Kataoka, D. Kosuge, K. Ogura, J. Ohyama, A. Satsuma, Reductive conversion of 5-hydroxymethylfurfural to 1,2,6-hexanetriol in water solvent using supported Pt catalysts, *Catal. Today* 352 (2020) 60–65, <https://doi.org/10.1016/j.cattod.2019.12.002>.
- [23] B. Pomeroy, M. Grilc, B. Likozar, Process condition-based tuneable selective catalysis of hydroxymethylfurfural (HMF) hydrogenation reactions to aromatic, saturated cyclic and linear poly-functional alcohols over Ni-Ce/Al₂O₃, *Green. Chem.* 23 (2021) 7996–8002, <https://doi.org/10.1039/d1gc02086b>.
- [24] J. Li, Y. Zhang, S. Xu, C. Hu, The roles of H₂O/tetrahydrofuran system in lignocellulose valorization, *Front. Chem.* 8 (2020), <https://doi.org/10.3389/fchem.2020.00070>.
- [25] G.M. Mullen, E.J. Evans, I. Sabzevari, B.E. Long, K. Alhazmi, B.D. Chandler, C. B. Mullins, Water influences the activity and selectivity of ceria-supported gold catalysts for oxidative dehydrogenation and esterification of ethanol, *ACS Catal.* 7 (2017) 1216–1226, <https://doi.org/10.1021/acscatal.6b02960>.
- [26] V.O.O. Gonçalves, C. Ciotonea, S. Arrii-Clacens, N. Guignard, C. Roudaut, J. Rousseau, J.M. Clacens, S. Royer, F. Richard, Effect of the support on the hydrodeoxygenation of m-cresol over molybdenum oxide based catalysts, *Appl. Catal. B Environ.* 214 (2017) 57–66, <https://doi.org/10.1016/j.apcatb.2017.05.003>.
- [27] H. Metiu, S. Chrétien, Z. Hu, B. Li, X. Sun, Chemistry of lewis acid-base pairs on oxide surfaces, *J. Phys. Chem. C* 116 (2012) 10439–10450, <https://doi.org/10.1021/jp301341t>.
- [28] S. Jiang, N. Ji, X. Diao, H. Li, Y. Rong, Y. Lei, Z. Yu, Vacancy engineering in transition metal sulfide and oxide catalysts for hydrodeoxygenation of lignin-derived oxygenates, *ChemSusChem* 14 (2021) 4377–4396, <https://doi.org/10.1002/cssc.202101362>.
- [29] C. Riley, A. De La Riva, S. Zhou, Q. Wan, E. Peterson, K. Artyushkova, M. D. Farahani, H.B. Friedrich, L. Burkemper, N.V. Atudorei, S. Lin, H. Guo, A. Datye, Synthesis of nickel-doped ceria catalysts for selective acetylene hydrogenation, *ChemCatChem* 11 (2019) 1526–1533, <https://doi.org/10.1002/cctc.201801976>.
- [30] J.F. Moulder, W.F. Stickle, P.E. Sobol, K.D. Bomben, *Handbook of X-ray Photoelectron Spectroscopy*, 1995.
- [31] T. Stroud, T.J. Smith, E. Le Saché, J.L. Santos, M.A. Centeno, H. Arellano-Garcia, J.A. Odriozola, T.R. Reina, Chemical CO₂ recycling via dry and bi reforming of methane using Ni-Sn/Al₂O₃ and Ni-Sn/CeO₂-Al₂O₃ catalysts, *Appl. Catal. B Environ.* 224 (2018) 125–135, <https://doi.org/10.1016/j.apcatb.2017.10.047>.
- [32] B. Zhang, S. Zhang, B. Liu, Effect of oxygen vacancies on ceria catalyst for selective catalytic reduction of NO with NH₃, *Appl. Surf. Sci.* 529 (2020), 147068, <https://doi.org/10.1016/j.apsusc.2020.147068>.
- [33] J. Zhang, H. Zhao, F. Wei, M. Yang, Z. Yang, Q. Chen, J. Chen, Resistive switching behaviour of highly epitaxial CeO₂ thin film for memory application, *Phys. Status Solidi - Rapid Res. Lett.* 8 (2014) 95–99, <https://doi.org/10.1002/pssr.201308158>.
- [34] X.H. Liu, W. Liu, X.K. Lv, F. Yang, X. Wei, Z.D. Zhang, D.J. Sellmyer, Magnetic properties of nickel hydroxide nanoparticles, *J. Appl. Phys.* 107 (2010), <https://doi.org/10.1063/1.3374468>.
- [35] K. Han, T. Kreuger, B. Mei, G. Mul, Transient behavior of Ni@NiOx functionalized SrTiO₃ in overall water splitting, *ACS Catal.* 7 (2017) 1610–1614, <https://doi.org/10.1021/acscatal.6b03662>.
- [36] D. Mukherjee, R. Singuru, P. Venkataswamy, D. Damma, B.M. Reddy, Ceria promoted Cu-Ni/SiO₂ catalyst for selective hydrodeoxygenation of vanillin, *ACS Omega* 4 (2019) 4770–4778, <https://doi.org/10.1021/acsomega.9b00039>.
- [37] R.W. Snell, B.H. Shanks, Ceria calcination temperature influence on acetic acid ketonization: Mechanistic insights, *Appl. Catal. A Gen.* 451 (2013) 86–93, <https://doi.org/10.1016/j.apcata.2012.08.043>.
- [38] G.B. Della Mea, L.P. Matte, A.S. Thill, F.O. Lobato, E.V. Benvenuti, L.T. Arenas, A. Jürgensen, R. Hergenröder, F. Poletto, F. Bernardi, Tuning the oxygen vacancy population of cerium oxide (CeO_{2-x}, 0 < x < 0.5) nanoparticles, *Appl. Surf. Sci.* 422 (2017) 1102–1112, <https://doi.org/10.1016/j.apsusc.2017.06.101>.
- [39] K. Wu, L.D. Sun, C.H. Yan, Recent progress in well-controlled synthesis of ceria-based nanocatalysts towards enhanced catalytic performance, *Adv. Energy Mater.* 6 (2016), <https://doi.org/10.1002/aenm.201600501>.
- [40] L. Wang, Y. Yu, H. He, Y. Zhang, X. Qin, B. Wang, Oxygen vacancy clusters essential for the catalytic activity of CeO₂ nanocubes for o-xylene oxidation, *Sci. Rep.* 7 (2017) 1–11, <https://doi.org/10.1038/s41598-017-13178-6>.
- [41] H. Wu, M. Zou, L. Guo, F. Ma, W. Mo, Y. Yu, I. Mian, J. Liu, S. Yin, N. Tsubaki, Effects of calcination temperatures on the structure-activity relationship of Ni-La/Al₂O₃ catalysts for syngas methanation, *RSC Adv.* 10 (2020) 3166–3174, <https://doi.org/10.1039/c9ra09674d>.
- [42] A.F. Lucrédio, G. Jerkiewicz, E.M. Assaf, Nickel catalysts promoted with cerium and lanthanum to reduce carbon formation in partial oxidation of methane reactions, *Appl. Catal. A Gen.* 333 (2007) 90–95, <https://doi.org/10.1016/j.apcata.2007.09.009>.
- [43] L. Pastor-Pérez, A. Sepúlveda-Escribano, Multicomponent NiSnCeO₂/C catalysts for the low-temperature glycerol steam reforming, *Appl. Catal. A Gen.* 529 (2017) 118–126, <https://doi.org/10.1016/j.apcata.2016.10.022>.
- [44] P.M. Shah, J.W.H. Burnett, D.J. Morgan, T.E. Davies, S.H. Taylor, Ceria–zirconia mixed metal oxides prepared via mechanochemical grinding of carbonates for the total oxidation of propane and naphthalene, *Catalysts* 9 (2019), <https://doi.org/10.3390/catal9050475>.
- [45] N.D. Charisiou, G.I. Siakavelas, B. Dou, V. Sebastian, S.J. Hinder, M.A. Baker, K. Polychronopoulou, M.A. Goula, Nickel supported on AlCeO₃ as a highly selective and stable catalyst for hydrogen production via the glycerol steam reforming reaction, *Catalysts* 9 (2019), <https://doi.org/10.3390/catal9050411>.
- [46] S. Damyanova, C.A. Perez, M. Schmal, J.M.C. Bueno, Characterization of ceria-coated alumina carrier, *Appl. Catal. A Gen.* 234 (2002) 271–282, [https://doi.org/10.1016/S0926-860X\(02\)00233-8](https://doi.org/10.1016/S0926-860X(02)00233-8).
- [47] K. Kamonsuangkasem, S. Therdthianwong, A. Therdthianwong, N. Thammajak, Remarkable activity and stability of Ni catalyst supported on CeO₂-Al₂O₃ via CeAlO₃ perovskite towards glycerol steam reforming for hydrogen production, *Appl. Catal. B Environ.* 218 (2017) 650–663, <https://doi.org/10.1016/j.apcatb.2017.06.073>.
- [48] X. Yang, J. Da, H. Yu, H. Wang, Characterization and performance evaluation of Ni-based catalysts with Ce promoter for methane and hydrocarbons steam reforming process, *Fuel* 179 (2016) 353–361, <https://doi.org/10.1016/j.fuel.2016.03.104>.
- [49] K.V. Manukyan, A.G. Avetisyan, C.E. Shuck, H.A. Chatilyan, S. Rouvimov, S. L. Kharatyan, A.S. Mukasyan, Nickel oxide reduction by hydrogen: kinetics and structural transformations, *J. Phys. Chem. C* 119 (2015) 16131–16138, <https://doi.org/10.1021/acs.jpcc.5b04313>.
- [50] I. Luisetto, S. Tuti, C. Battocchio, S. Lo Mastro, A. Sodo, Ni/CeO₂-Al₂O₃ catalysts for the dry reforming of methane: The effect of CeAlO₃ content and nickel crystallite size on catalytic activity and coke resistance, *Appl. Catal. A Gen.* 500 (2015) 12–22, <https://doi.org/10.1016/j.apcata.2015.05.004>.
- [51] B. Zhang, S. Zhang, B. Liu, Effect of oxygen vacancies on ceria catalyst for selective catalytic reduction of NO with NH₃, *Appl. Surf. Sci.* 529 (2020), 147068, <https://doi.org/10.1016/j.apsusc.2020.147068>.
- [52] H. Arbag, H.M. Tasdemir, Y. Yagizatl, M. Kucuker, S. Yasyerli, Effect of preparation technique on the performance of Ni and Ce incorporated modified alumina catalysts in CO₂ reforming of methane, *Catal. Lett.* 150 (2020) 3256–3268, <https://doi.org/10.1007/s10562-020-03228-6>.
- [53] Y. Wang, F. Wang, Q. Song, Q. Xin, S. Xu, J. Xu, Heterogeneous ceria catalyst with water-tolerant Lewis acidic sites for one-pot synthesis of 1,3-diols via prins condensation and hydrolysis reactions, *J. Am. Chem. Soc.* 135 (2013) 1506–1515, <https://doi.org/10.1021/ja310498c>.
- [54] J. He, M.R. Nielsen, T.W. Hansen, S. Yang, A. Riisager, Hierarchically constructed NiO with improved performance for catalytic transfer hydrogenation of biomass-derived aldehydes, *Catal. Sci. Technol.* 9 (2019) 1289–1300, <https://doi.org/10.1039/c8cy02536c>.
- [55] M. Li, J. Fu, S. Xing, L. Yang, X. Zhang, P. Lv, Z. Wang, Z. Yuan, A novel catalyst with variable active sites for the direct hydrogenation of waste oils into jet fuel, *Appl. Catal. B Environ.* 260 (2020), 118114, <https://doi.org/10.1016/j.apcatb.2019.118114>.
- [56] M.M. Mohamed, Effect of ceria-doped titania on the structure and acidic properties of MoO₃/TiO₂ catalysts, *Appl. Catal. A Gen.* 267 (2004) 135–142, <https://doi.org/10.1016/j.apcata.2004.02.034>.
- [57] Z. Liang, D. Jiang, G. Fang, W. Leng, P. Tu, Y. Tong, L. Liu, J. Ni, X. Li, Catalytic enhancement of aldol condensation by oxygen vacancy on CeO₂ catalysts, *ChemistrySelect* 4 (2019) 4364–4370, <https://doi.org/10.1002/slct.201900712>.

- [58] S. Ewald, Applied catalysis A, general on the interaction of CO₂ with Ni-Al catalysts, *Appl. Catal. A, Gen.* 580 (2019) 71–80, <https://doi.org/10.1016/j.apcata.2019.04.005>.
- [59] J. Szanyi, J.H. Kwak, Dissecting the steps of CO₂ reduction: 2. The interaction of CO and CO₂ with Pd/ γ -Al₂O₃: An in situ FTIR study, *Phys. Chem. Chem. Phys.* 16 (2014) 15126–15138, <https://doi.org/10.1039/c4cp00617h>.
- [60] J. Szanyi, J.H. Kwak, Dissecting the steps of CO₂ reduction: 1. The interaction of CO and CO₂ with γ -Al₂O₃: An in situ FTIR study, *Phys. Chem. Chem. Phys.* 16 (2014) 15117–15125, <https://doi.org/10.1039/c4cp00616j>.
- [61] N.V. Vlasenko, P.I. Kyriienko, O.I. Yanushevska, K.V. Valihura, S.O. Soloviev, P. E. Strizhak, The effect of ceria content on the acid–base and catalytic characteristics of ZrO₂–CeO₂ oxide compositions in the process of ethanol to n-butanol condensation, *Catal. Lett.* 150 (2020) 234–242, <https://doi.org/10.1007/s10562-019-02937-x>.
- [62] A. Holmgren, B. Andersson, D. Duprez, *Interact. CO Pt / Ceria Catal.* 22 (1999) 215–230.
- [63] Y. Denkwitz, A. Karpenko, V. Plzak, R. Leppelt, B. Schumacher, R.J. Behm, Infl. CO₂ H₂. 2 Low. -Temp. Water – Gas. shift React. Au / CeO₂ Catal. Ideal. Realistic Reforma 246 (2007) 74–90, <https://doi.org/10.1016/j.jcat.2006.11.012>.
- [64] M.V. Konishcheva, D.I. Potemkin, S.D. Badmaev, P.V. Snytnikov, On the Mechanism of CO and CO₂ Methanation Over Ni / CeO₂, *Catalysts* (2016) 1424–1430, <https://doi.org/10.1007/s11244-016-0650-7>.
- [65] L. Sergio, A. Dav, E. Bail, D. Lozano-castell, F.C. Herrera, E. Pellegrin, C. Escudero, M. Garc, Elucidating Role Met. Catal. Oxide Support Ru / CeO₂ – Catalyzed CO₂ Methanation Mech. (2021), <https://doi.org/10.1021/acs.jpcc.1c07537>.
- [66] K. Lorber, J. Zavašnik, I. Arčon, M. Huš, J. Teržan, B. Likozar, P. Djinić, CO₂ Activation over Nanoshaped CeO₂ Decorated with Nickel for Low-Temperature Methane Dry Reforming, *ACS Appl. Mater. Interfaces* 14 (2022) 31862–31878, <https://doi.org/10.1021/acsami.2c05221>.
- [67] S.H. Krishna, D.J. McClelland, Q.A. Rashke, J.A. Dumesic, G.W. Huber, Hydrogenation of levoglucosenone to renewable chemicals, *Green. Chem.* 19 (2017) 1278–1285, <https://doi.org/10.1039/c6gc03028a>.
- [68] Y.L. Louie, J. Tang, A.M.L. Hell, A.T. Bell, Kinetics of hydrogenation and hydrogenolysis of 2,5-dimethylfuran over noble metals catalysts under mild conditions, *Appl. Catal. B Environ.* 202 (2017) 557–568, <https://doi.org/10.1016/j.apcatb.2016.09.046>.
- [69] T. Buntara, S. Noel, P.H. Phua, I. Melián-Cabrera, J.G. De Vries, H.J. Heeres, From 5-hydroxymethylfurfural (HMF) to polymer precursors: Catalyst screening studies on the conversion of 1,2,6-hexanetriol to 1,6-hexanediol, *Top. Catal.* 55 (2012) 612–619, <https://doi.org/10.1007/s11244-012-9839-6>.
- [70] J. Tuteja, H. Choudhary, S. Nishimura, K. Ebitani, Direct synthesis of 1,6-hexanediol from HMF over a heterogeneous Pd/ZrP catalyst using formic acid as hydrogen source, *ChemSusChem* 7 (2014) 96–100, <https://doi.org/10.1002/cssc.201300832>.
- [71] Y.L. Louie, J. Tang, A.M.L. Hell, A.T. Bell, Kinetics of hydrogenation and hydrogenolysis of 2,5-dimethylfuran over noble metals catalysts under mild conditions, *Appl. Catal. B Environ.* 202 (2017) 557–568, <https://doi.org/10.1016/j.apcatb.2016.09.046>.
- [72] J. Luo, M. Monai, H. Yun, L. Arroyo-Ramírez, C. Wang, C.B. Murray, P. Fornasiero, R.J. Gorte, The H₂ pressure dependence of hydrodeoxygenation selectivities for furfural over Pt/C catalysts, *Catal. Lett.* 146 (2016) 711–717, <https://doi.org/10.1007/s10562-016-1705-x>.
- [73] T. Panczyk, P. Szabelski, W. Rudzinski, Hydrogen adsorption on nickel (100) single-crystal face. a Monte Carlo, Study Equilib. Kinet., *J. Phys. Chem. B* 109 (2005) 10986–10994, <https://doi.org/10.1021/jp047230a>.
- [74] Z. Zhang, X. Zhou, C. Liu, J. Guo, H. Ning, Hydrogen adsorption and dissociation on nickel-adsorbed and -substituted Mg17Al12 (100) surface: a density functional theory study, *Int. J. Hydrog. Energy* 43 (2018) 793–800, <https://doi.org/10.1016/j.ijhydene.2017.11.004>.
- [75] E. Brunner, Solubility of Hydrogen in 10 Organic Solvents at 298.15, 323.15, and 373.15 K, *J. Chem. Eng. Data* 30 (1985) 269–273, <https://doi.org/10.1021/je00041a010>.
- [76] M. Grile, B. Likozar, Levulinic acid hydrodeoxygenation, decarboxylation and oligomerization over NiMo/Al₂O₃ catalyst to bio-based value-added chemicals: Modelling of mass transfer, thermodynamics and micro-kinetics, *Chem. Eng. J.* 330 (2017) 383–397, <https://doi.org/10.1016/j.cej.2017.07.145>.
- [77] J. Chen, R. Liu, Y. Guo, L. Chen, H. Gao, Selective hydrogenation of biomass-based 5-hydroxymethylfurfural over catalyst of palladium immobilized on amine-functionalized metal-organic frameworks, *ACS Catal.* 5 (2015) 722–733, <https://doi.org/10.1021/acs Catal.5012926>.
- [78] J. Long, Y. Xu, W. Zhao, H. Li, S. Yang, Heterogeneous catalytic upgrading of biofuranic aldehydes to alcohols, *Front. Chem.* 7 (2019), <https://doi.org/10.3389/fchem.2019.00529>.
- [79] L. Faba, E. Díaz, S. Ordóñez, Hydrodeoxygenation of acetone-furfural condensation adducts over alumina-supported noble metal catalysts, *Appl. Catal. B Environ.* 160 161 (2014) 436–444, <https://doi.org/10.1016/j.apcatb.2014.05.053>.
- [80] Z. Huang, X. Sun, W. Zhao, X. Zhu, Z. Zeng, Q. Xu, X. Liu, Selective hydroconversion of 5-hydroxymethylfurfural to 2,5-bis(hydroxymethyl)furan using carbon nanotubes-supported nickel catalysts, *Carbon Resour. Convers.* 5 (2022) 289–298, <https://doi.org/10.1016/j.crccon.2022.08.001>.
- [81] Z. Liu, Z. Huang, W. Zhao, X. Liu, Highly efficient Ni-NiO/carbon nanotubes catalysts for the selective transfer hydrogenation of 5-hydroxymethylfurfural to 2,5-bis(hydroxymethyl)furan, *React. Chem. Eng.* 7 (2022) 1873–1878, <https://doi.org/10.1039/d2re00134a>.
- [82] K.T.V. Rao, Y. Hu, Z. Yuan, Y. Zhang, C.C. Xu, Green synthesis of heterogeneous copper-alumina catalyst for selective hydrogenation of pure and biomass-derived 5-hydroxymethylfurfural to 2,5-bis(hydroxymethyl)furan, *Appl. Catal. A Gen.* 609 (2021), 117892, <https://doi.org/10.1016/j.apcata.2020.117892>.
- [83] X. Kong, Y. Zhu, H. Zheng, X. Li, Y. Zhu, Y.W. Li, Ni Nanoparticles Inlaid Nickel Phyllosilicate as a Metal-Acid Bifunctional Catalyst for Low-Temperature Hydrogenolysis Reactions, *ACS Catal.* 5 (2015) 5914–5920, <https://doi.org/10.1021/acs Catal.5b01080>.
- [84] W. Song, Y. Liu, E. Baráth, C. Zhao, J.A. Lercher, Synergistic effects of Ni and acid sites for hydrogenation and C–O bond cleavage of substituted phenols, *Green. Chem.* 17 (2015) 1204–1218, <https://doi.org/10.1039/C4GC01798F>.
- [85] M.R. Nolan, A. Bejile, S.L. Enombo, B.H. Shanks, Directing polyol dehydration via modification of acid catalysts with metals, *Top. Catal.* 59 (2016) 29–36, <https://doi.org/10.1007/s11244-015-0502-x>.
- [86] C.E. Bounoukta, C. Megías-Sayago, F. Ammiri, S. Ivanova, A. Monzon, M. A. Centeno, J.A. Odriozola, Dehydration of glucose to 5-Hydroxymethylfurfural on bifunctional carbon catalysts, *Appl. Catal. B Environ.* 286 (2021), <https://doi.org/10.1016/j.apcatb.2021.119938>.
- [87] J. Mitra, X. Zhou, T. Rauchfuss, Pd/C-catalyzed reactions of HMF: decarbonylation, hydrogenation, and hydrogenolysis, *Green. Chem.* 17 (2015) 307–313, <https://doi.org/10.1039/c4gc01520g>.
- [88] M. Chidambaram, A.T. Bell, A two-step approach for the catalytic conversion of glucose to 2,5-dimethylfuran in ionic liquids, *Green. Chem.* 12 (2010) 1253–1262, <https://doi.org/10.1039/c004343e>.
- [89] S. Yao, X. Wang, Y. Jiang, F. Wu, X. Chen, X. Mu, One-step conversion of biomass-derived 5-hydroxymethylfurfural to 1,2,6-hexanetriol over ni-co-al mixed oxide catalysts under mild conditions, *ACS Sustain. Chem. Eng.* 2 (2014) 173–180, <https://doi.org/10.1021/sc4003714>.
- [90] B. Zhang, Y. Zhu, G. Ding, H. Zheng, Y. Li, Selective conversion of furfuryl alcohol to 1,2-pentanediol over a Ru/MnOx catalyst in aqueous phase, *Green. Chem.* 14 (2012) 3402–3409, <https://doi.org/10.1039/c2gc36270h>.
- [91] J. Saavedra, H.A. Doan, C.J. Pursell, L.C. Grabow, B.D. Chandler, The critical role of water at the gold-titania interface in catalytic CO oxidation, *Sci. (80-.)* 345 (2014) 1599–1602, <https://doi.org/10.1126/science.1256018>.
- [92] J. Saavedra, C. Powell, B. Panthi, C.J. Pursell, B.D. Chandler, CO oxidation over Au/TiO₂ catalyst: Pretreatment effects, catalyst deactivation, and carbonates production, *J. Catal.* 307 (2013) 37–47, <https://doi.org/10.1016/j.jcat.2013.06.021>.
- [93] Q. Xu, Y. Shi, L. Yang, G. Fan, F. Li, The promotional effect of surface Ru decoration on the catalytic performance of Co-based nanocatalysts for guaiacol hydrodeoxygenation, *Mol. Catal.* 497 (2020), 111224, <https://doi.org/10.1016/j.mcat.2020.111224>.
- [94] M.K. Gnanamani, R. Garcia, G. Jacobs, K. Góra-Marek, D.C. Cronauer, A.J. Kropf, C.L. Marshall, Effect of pretreatment conditions on acidity and dehydration activity of CeO₂-MeOx catalysts, *Appl. Catal. A Gen.* 602 (2020), <https://doi.org/10.1016/j.apcata.2020.117722>.
- [95] A. Salcedo, E. Poggio-Fraccari, F. Mariño, B. Irigoyen, Tuning the selectivity of cerium oxide for ethanol dehydration to ethylene, *Appl. Surf. Sci.* 599 (2022), <https://doi.org/10.1016/j.apsusc.2022.153963>.
- [96] H. Heydari, M.R. Elahifard, R. Behjatmanesh-Ardakani, Role of oxygen vacancy in the adsorption and dissociation of the water molecule on the surfaces of pure and Ni-doped rutile (110): a periodic full-potential DFT study, *Surf. Sci.* 679 (2019) 218–224, <https://doi.org/10.1016/j.susc.2018.09.014>.
- [97] T. Sarkar, S. Ghosh, M. Annamalai, A. Patra, K. Stoerzinger, Y.L. Lee, S. Prakash, M.R. Motapothula, Y. Shao-Horn, L. Giordano, T. Venkatesan, The effect of oxygen vacancies on water wettability of transition metal based SrTiO₃ and rare-earth based Lu₂O₃, *RSC Adv.* 6 (2016) 109234–109240, <https://doi.org/10.1039/c6ra22391e>.
- [98] Q. Wang, A. Puntambekar, V. Chakrapani, Gaseous reactions in adsorbed water present on transition metal oxides, *J. Phys. Chem. C* 121 (2017) 13151–13163, <https://doi.org/10.1021/acs.jpcc.7b02173>.
- [99] T. Zhang, C. Li, J. Ma, H. Tian, Z. Qiang, Surface hydroxyl groups of synthetic α -FeOOH in promoting OH generation from aqueous ozone: Property and activity relationship, *Appl. Catal. B Environ.* 82 (2008) 131–137, <https://doi.org/10.1016/j.apcatb.2008.01.008>.
- [100] L.G.M. Pettersson, T. Schiros, H. Ogasawara, L.A. Näslund, K.J. Andersson, J. Ren, S. Meng, G.S. Karlberg, M. Odelius, A. Nilsson, Cooperativity in surface bonding and hydrogen bonding of water and hydroxyl at metal surfaces, *J. Phys. Chem. C* 114 (2010) 10240–10248, <https://doi.org/10.1021/jp101855v>.
- [101] Q. Meng, D. Cao, G. Zhao, C. Qiu, X. Liu, X. Wen, Y. Zhu, Y. Li, The role of water on the selective decarbonylation of 5-hydroxymethylfurfural over Pd/Al₂O₃ catalyst: experimental and DFT studies, *Appl. Catal. B Environ.* 212 (2017) 15–22, <https://doi.org/10.1016/j.apcatb.2017.04.069>.
- [102] Z. Zhao, R. Bababrik, W. Xue, Y. Li, N.M. Briggs, D.T. Nguyen, U. Nguyen, S. P. Crossley, S. Wang, B. Wang, D.E. Resasco, Solvent-mediated charge separation drives alternative hydrogenation path of furanics in liquid water, *Nat. Catal.* 2 (2019) 431–436, <https://doi.org/10.1038/s41929-019-0257-z>.
- [103] G. Li, B. Wang, D.E. Resasco, Water-mediated heterogeneously catalyzed reactions, *ACS Catal.* 10 (2020) 1294–1309, <https://doi.org/10.1021/acscatal.9b04637>.
- [104] S. Chen, C. Ciotonea, K.D.O. Vigier, F. Jérôme, R. Wojcieszak, F. Dumeignil, E. Marceau, S. Royer, S. Chen, C. Ciotonea, K.D.O. Vigier, F. Jérôme, R. Wojcieszak, Hydroconversion 5-Hydroxymethylfurfural Non-Promot. Ni / SBA-15 cite this Version: Hal. Id: Hal. -02906610 (2020).
- [105] W. Zhao, Z. Huang, L. Yang, X. Liu, H. Xie, Z. Liu, Highly efficient syntheses of 2,5-bis(hydroxymethyl)furan and 2,5-dimethylfuran via the hydrogenation of

- biomass-derived 5-hydroxymethylfurfural over a nickel–cobalt bimetallic catalyst, *Appl. Surf. Sci.* 577 (2022), 151869, <https://doi.org/10.1016/j.apsusc.2021.151869>.
- [106] L.F. Lundegaard, R.R. Tiruvalam, C. Tyrsted, A. Carlsson, F. Morales-Cano, C. V. Ovesen, Migrating Al species hindering NiO reduction on Al containing catalyst carriers, *Catal. Today* 272 (2016) 25–31, <https://doi.org/10.1016/j.cattod.2015.08.055>.
- [107] J. Du, J. Gao, F. Gu, J. Zhuang, B. Lu, L. Jia, G. Xu, Q. Liu, F. Su, A strategy to regenerate coked and sintered Ni/Al₂O₃ catalyst for methanation reaction, *Int. J. Hydrog. Energy* 43 (2018) 20661–20670, <https://doi.org/10.1016/j.ijhydene.2018.09.128>.